

# Preferential Hydrologic States and Tipping Characteristics of Global Surface Soil Moisture

Vinit Sehgal<sup>1,2</sup> and Binayak P Mohanty<sup>2</sup>

<sup>1</sup>Water Management and Hydrological Science, Texas A& M University

<sup>2</sup>Biological and Agricultural Engineering, Texas A&M University

March 9, 2023

# Preferential Hydrologic States and Tipping Characteristics of Global Surface Soil Moisture

Vinit Sehgal<sup>1,2</sup>, Binayak P. Mohanty<sup>2</sup>

<sup>1</sup>Water Management and Hydrological Science, Texas A& M University, TX 77843, USA

<sup>2</sup>Biological and Agricultural Engineering, Texas A&M University, TX 77843, USA.

## Key Points:

- Global surface soil moisture dynamics is categorized into dry-preferential, wet-preferential and bistable hydrologic states
- Tipping characteristics are defined to capture intensity, frequency, and duration of surface soil moisture excursions from wet- to dry-average state
- Tipping characteristics capture soil–vegetation–climate coexistence patterns within global biomes

**Keywords:** SMAP; surface soil moisture; soil moisture preferential states; tipping characteristics, soil moisture drydowns, soil water retention parameters

---

Corresponding author: Binayak P. Mohanty, [bmohanty@tamu.edu](mailto:bmohanty@tamu.edu)

## Abstract

A dynamic transition in soil hydrologic states through climate perturbations and terrestrial feedbacks governs soil-vegetation-climate (SVC) interactions, constrained by critical soil moisture (SM) thresholds. Observational and scaling constraints limit critical SM threshold estimation at the remote-sensing (RS) footprint scale. Using global surface SM ( $\theta_{RS}$ ) from NASA's Soil Moisture Active Passive (SMAP) satellite, we characterize seasonal preferential hydrologic states of  $\theta_{RS}$  and derive three tipping characteristics to estimate the intensity (Mean Tipping Depth,  $\bar{\epsilon}$ ), frequency (Tipping Count,  $\eta$ ), and duration (Mean Tipped Time,  $\bar{\tau}$ ) of the excursion of  $\theta_{RS}$  from wet- to dry-average conditions. The preferential state provides the seasonally dominant hydrological states of  $\theta_{RS}$ , while tipping characteristics capture the ecosystem linkages of the dynamic transition in  $\theta_{RS}$  hydrologic states. Globally,  $\theta_{RS}$  predominantly exhibits a (unimodal) dry-preferential state, especially over arid/ semi-arid drylands and a unimodal wet-preferential  $\theta_{RS}$  state in high-latitude boreal forests and tundra biomes. Prevalence of (bimodal) bistable  $\theta_{RS}$  state overlaps with regions of strong positive SM-precipitation coupling and monsoonal climate in semi-arid/ subhumid climates. Seasonal preferential hydrologic states co-vary with the regional variability in plant water stress threshold and land-atmospheric coupling strength. Tipping characteristics of  $\theta_{RS}$  show sensitivity to intra-biome variability in SVC coexistence patterns and display high skill in partitioning global ecoregions. While  $\bar{\epsilon}$  and  $\eta$  are climate-controlled,  $\bar{\tau}$  is moderated by soil and vegetation through their influence over  $\theta_{RS}$  drydown during Stage II evapotranspiration. Preferential states and tipping characteristics find applications in quantifying SVC coexistence patterns, climate model diagnosis, and assessing ecosystem sensitivity to climate change.

## 1 Introduction

The nature of the SVC interactions evolves with changing SM, where certain soil water retention parameters (SWRPs) demarcate the dominant soil hydrologic processes (Porporato et al., 2002; Rodriguez-Iturbe, 2000). Below a certain threshold SM called the critical point, the SVC system is considered moisture limited. In this regime, evapotranspiration (ET) is constrained by the SM availability, which contributes to an increased land-surface temperature and initiates a positive land-atmospheric feedback (Pendergrass et al., 2020). As the SM decreases further, vegetation stress increases, and plants lose turgor as SM falls below the wilting point (Porporato et al., 2002). Energy-limited SVC systems (when  $SM >$  critical point) are characterized by weakened linkages between water-carbon-energy cycles due to limiting net radiation and atmospheric resistance (as opposed to SM), with ET losses close to (or at) the potential rate (Fu et al., 2021). A seamless and accurate estimation of the global thresholds of soil hydrologic regimes is important as the sensitivity and resilience of the SVC system to climatic fluctuation are linked to the transient shifts of SM state within contrasting hydrologic regimes.

At the RS-footprint scale, several observational and scale-related constraints limit the identification and threshold estimation of the soil hydrologic regimes— thereby limiting the prospects of quantifying the dynamic shift of SM between hydrologic states and their eco-hydrological impacts. Recent studies have highlighted these concerns while parameterizing the pathway of SM drydowns (Akbar et al., 2018; Sehgal et al., 2021b) or by leveraging land-surface energy partitioning (Feldman et al., 2019) using satellite SM ( $\theta_{RS}$ ) observations. Variable precipitation or irrigation patterns within the RS-footprint, along with subgrid-scale heterogeneity in soil, vegetation and topography yields a non-unique relationship between the footprint-mean SM and the net observed rate of SM loss (Sehgal et al., 2021b). This leads to high uncertainty in estimating RS-footprint scale effective SWRPs, especially over croplands, grasslands, and savannah ecosystems. Simpler functional forms of drydown pathways are preferred to prevent overparameterization of drydown curves under such uncertainty, which often captures fewer hydrological regimes. Moreover, a revisit time of 2-3 days (for SMAP) often misses transient processes like gravity drainage (McColl et al., 2017). Arid climates are characterized by the prevalence of transitional or dry hydrologic regimes, where precipitation events are too short and sparse for accurate identification of the energy-limited hydrological regimes.

The linkages of soil water balance to noise-induced variability in the climatic forcings and positive land-atmospheric feedback cause a dynamic inter-state transition of SM, which may yield a preferential hydrologic state at a seasonal scale (Rodriguez-Iturbe et al., 1991; Entekhabi et al., 1992, 1996). As one or more state variables are perturbed, or stress (at-

atmospheric moisture demand causing evapotranspirative losses) is incrementally altered, the SVC system may shift (or “tip”) into a new regime (D’Odorico & Porporato, 2004). Sustainment of dry-average condition reinforces dry anomalies (low evaporation leads to low regional precipitation and dry soils, and hence, lower evaporation). In contrast, precipitation can shift soil hydrologic state to the wet-average conditions, thereby increasing regional evaporation, and thus, precipitation through moisture recycling. This bistability in the deterministic processes governing SM dynamics may manifest as bimodality in the SM density distribution (Cueto-Felgueroso et al., 2015; Scheffer et al., 2001). Bistability (and corresponding bimodality) in SM dynamics is reported by stochastic soil water balance studies (Yin et al., 2014), soil-atmosphere-vegetation models (Nishat et al., 2007; Settin et al., 2007; Baudena et al., 2008) and field/ point scale observations (E. Lee & Kim, 2022; T. R. Lee & Hornberger, 2006; Nishat et al., 2007; Teuling, 2005). In contrast, studies on SM bimodality at the RS-footprint scale remain extremely limited (Vilasa et al., 2017).

Tipping characteristics of SM moderate the ability of land-atmosphere interactions to enhance and sustain droughts and floods, including the severity of their effects (Oglesby, 2002). The dynamics of the ecosystem tipping from the equilibrium to the preferential states that favor or limits the growth of a plant species has implications on the dominance and structure of the plant ecosystems through control over transpiration rate, biomass production, and carbon assimilation (D’Odorico et al., 2000). Hence, diverse applications of SM tipping characteristics (referred to as crossing properties in Tamea et al. (2011) are shown in literature, including the estimation of dynamic plant water stress (Porporato et al., 2002; Rodríguez-Iturbe et al., 2001), SM memory (Ghannam et al., 2016; Jacobs et al., 2020), landslide potential (Ray et al., 2011), infiltration and leaching (Manfreda et al., 2009), and patterns of drought susceptibility and recovery of plants (Rodríguez-Iturbe & Porporato, 2007) etc. As soil hydrologic states and the dynamic shift of SM therewithin are intrinsically linked to climatic perturbations and dynamic vegetation stress, tipping characteristics of SM can be important indicator of ecosystem sensitivity to climate change. Recent studies have used the fraction of time spent by  $\theta_{RS}$  in the water-limited regime as a measure of SM responsiveness to atmospheric forcing (Feldman et al., 2019, 2022). However, a comprehensive assessment of the tipping characteristics of  $\theta_{RS}$ , their controls, and ecohydrological implications at a global scale remains largely unavailable.

In this study, we argue that the preferential states provide a probabilistic approach of ascribing seasonally dominant soil hydrological processes to a RS-footprint using  $\theta_{RS}$  observations in terms of dry-average (likely moisture-limited) and wet-average (likely energy-limited) conditions. While the challenges in estimating SWRPs from  $\theta_{RS}$  persist due to observational or scaling constraints at the RS-footprint scale, we use preferential hydrologic

states as an alternative to SWRPs to characterize the dynamic transition of global  $\theta_{RS}$  from wet- to dry-average conditions. The objectives of this study are to: *i*) identify the seasonal preferential hydrological states of global  $\theta_{RS}$  at RS-footprint scale, *ii*) estimate the respective tipping characteristics of the dynamic transition of from wet- to dry-average state and *iii*) study the ecohydrological linkages of preferential soil hydrologic states and tipping characteristics. The shift of  $\theta_{RS}$  into wet-average conditions is primarily driven by transient and stochastic atmospheric drivers, while the dry-tipping characteristics (during  $\theta_{RS}$  drydowns) can capture the impact of vegetation, soil hydraulic properties and footprint scale variability of land-surface characteristics. Hence we focus on the dry-tipping properties in this study. The footprint-scale density distribution of  $\theta_{RS}$  is parameterized as a unimodal truncated gamma or a bimodal mixture of truncated gamma models. Based on the distribution characteristics, the preferential hydrological state of footprint-scale  $\theta_{RS}$  is classified as a dry-preferential, wet-preferential, or bistable. We estimate three tipping characteristics representing the intensity, frequency, and duration of the excursions of  $\theta_{RS}$  from wet- to dry-average condition. A global analysis is carried out to study the soil, vegetation, and climate controls on  $\theta_{RS}$  tipping characteristics and demonstrate their sensitivity to the coexistence patterns of soil-vegetation-climate within (global) ecoregions.

## 2 Dataset

### 2.1 SM observations from SMAP ( $\theta_{RS}$ )

We use 6.5 years of global surface (0-5 cm) SM observations from NASA’s Soil Moisture Active Passive (SMAP) satellite (level 3, version 7) from 31<sup>st</sup> March 2015 to 30<sup>th</sup> September 2021. SMAP uses an L-band (1.41 GHz) microwave radiometer with footprint of  $\sim 40$  KM re-sampled to 36 KM (nested) Equal-Area grids, and has a global revisit period of 2-3 days (Entekhabi et al., 2010; O’Neill, 2018). Improved land surface temperature correction in the latest versions of SMAP enables both descending (6 A.M.) and ascending overpass (6 P.M.) retrievals to meet the mission accuracy target of  $\pm 0.04 \text{ cm}^3/\text{cm}^3$  unbiased root mean squared error for unfrozen land surfaces (Jackson et al., 2018; O’Neill, 2018). SMAP data is quality-screened for high water fraction ( $>1\%$ ), radio frequency interference and high vegetation water content ( $>7 \text{ kg/m}^2$ , following Sehgal et al. (2021b, 2021a)), snow cover, flooding, large and highly variable slopes, and urban sprawl. Quality-screened SMAP observations from the ascending and descending overpass are linearly interpolated and thinned to a uniform 2-days (6 A.M. local time) sampling frequency to counter the influence of diurnal variability in  $\theta_{RS}$ . SMAP retrievals are limited by a small dynamic range, high noise, and dry-bias over hyper-arid regions like the Arabian peninsula and Sahara desert (Burgin et al., 2017; Kolassa et al., 2018; Reichle et al., 2015) and hence, are not considered for the analysis.

## 2.2 Ancillary datasets

Aridity Index (AI) is defined as the ratio of the mean annual precipitation and reference evapotranspiration. We use global AI estimates obtained from the Global Aridity Index and Potential Evapotranspiration (ET<sub>0</sub>) Climate Database (version 2), which uses climate records from 1970-2000 (Fick & Hijmans, 2017; Zomer et al., 2022). AI is divided into five climate classes, namely, hyper-arid (AI < 0.05, excluded from the analysis), arid (0.05 ≤ AI < 0.20), semi-arid (0.20 ≤ AI < 0.50), dry-subhumid (0.50 ≤ AI < 0.65) and humid (0.65 ≤ AI) as prescribed by UNEP (1997). We use global terrestrial classification of biomes (n = 14) and ecoregions (n = 867) from Olson et al. (2001). Ecoregions approximate the area where the assemblages of ecological processes most strongly interact within a biome, prior to major land-use change. Classification of these ecoregions is based on several bio-geo-physical features including (but not limited to) climate, landforms, vegetation, phytogeography, biogeography, biotic provinces, fire disturbance regimes (Smith et al., 1998; Zhou et al., 2003), and thus, account for the dynamic SVC interactions. Ecoregion based approach is demonstrated to have strong linkages to SM dynamics (Baldwin et al., 2017), soil organic carbon dynamics (Endsley et al., 2020), plant water storage and hydraulics (Tian et al., 2018), and watershed organic carbon flux transport (Zarnetske et al., 2018). Global soil textural estimates are taken from SoilGrids250 (Hengl et al., 2017), which are bilinearly resampled to match the SMAP footprint.

## 3 Methodology

### 3.1 Density distribution of seasonal $\theta_{RS}$

We assume that the probability density of  $\theta_{RS}$  is adequately represented using either a unimodal Truncated-Gamma (TG) or a Truncated-Gamma Mixture (TGM) distribution. A TG distribution is defined for  $0 < \theta_{RS} < 1$  with a shape ( $\alpha$ ) and a rate ( $\beta$ ) parameter in Eq. 1 as:

$$p(\theta_{RS}) = \frac{\beta^\alpha}{\Gamma(\alpha) - \Gamma(\alpha, \beta)} \theta_{RS}^{\alpha-1} e^{-\beta \cdot \theta_{RS}} \quad (1)$$

where,  $\Gamma(\cdot)$  and  $\Gamma(\cdot, \cdot)$  are the complete and incomplete gamma functions respectively (Abramowitz et al., 1988). The TGM models are bimodal distributions defined by five parameters, namely, the shape and rate parameters of the two constituent TG models, and the mixing ratio. To capture the temporal variability in the  $\theta_{RS}$  distribution, distribution functions are fitted on seasonal  $\theta_{RS}$  observations for each pixel. Seasons are defined as, *i*) December-February (DJF), *ii*) March-May (MAM), *iii*) June-August (JJA), and *iv*)

September-November, (SON) corresponding to boreal winter, spring, summer and fall respectively. The choice of TG distribution (or a mixture thereof) for modeling  $\theta_{RS}$  density is based on probabilistic soil water balance studies where the steady-state density distribution of SM is observed to take the form of a TG distribution (Feng et al., 2015; Porporato et al., 2004; Rodriguez-Iturbe et al., 1999). TG are robust models, which can represent  $\theta_{RS}$  densities in different climatic conditions, including when  $\theta_{RS}$  distribution may be prone to high skewness, for example, in arid and humid climates (Porporato et al., 2004). Assuming  $p(\theta_{RS}|\omega_k)$  represents a unimodal TG distribution of  $\theta_{RS}$  with parameter set  $\omega_k = (\alpha_k, \beta_k)$ , TGM models are given by  $P(\theta_{RS}|\omega_k)$  in Eq. 2 as:

$$P(\theta_{RS} | \omega) = \sum_{k=1}^K w_k p(\theta_{RS} | \omega_k) \quad (2)$$

where  $w_k$  are the mixing ratios,  $K$ = number of mixture components (=2 in this study), with constraints  $0 \leq w_k \leq 1$  and  $\sum_{k=1}^K w_k = 1$ . We follow the maximum-likelihood estimation using Expectation-Maximization (EM) algorithm to estimate the parameters of the mixed distribution functions. Details of these algorithms are provided in the Sections S1 and S2 of the Supplementary material. For the ease of interpretation, the mixture densities,  $p(\theta_{RS} | \omega_{k=1,2})$ , are differentiated as  $p_{dry}$  and  $p_{wet}$  with modes  $MO_{dry}$  and  $MO_{wet}$  respectively, where  $MO_{wet} > MO_{dry}$ .

Pixel-wise selection of best fitting model among TG and TGM models is carried out to classify each pixel into unimodal or bimodal density distribution. For completeness, the fitting performance of TGM and TG models is compared with several other models selected based on literature review including Truncaed Weibull, Truncated Normal, and Beta and Beta Mixture models (Famiglietti et al., 2008; Sadri et al., 2020; Sheffield, 2004). The comparison shows that depending on the season, TG and TGM models provide satisfactory fitting performance for  $\theta_{RS}$  for 72-82% of the evaluated pixels (Figures S1 and S2 of the Supplementary material). Hence, only TG and TGM models are used for the analysis for simplicity in this study.

### 3.2 Test for bimodality

We perform a pixel-wise comparison of the fitting performance of TG and TGM models to evaluate the best-fit model for  $\theta_{RS}$  using Akaike information criterion (AIC). AIC is calculated as,  $AIC=2k-2 \ln(L)$ , where, L is the maximum value of the likelihood function of the model and k is the number of model parameters. To prevent overfitting, preference is given to the 2-parameter TG models when  $(AIC_{TGM}-AIC_{TG}) \leq 7$ . The threshold difference of 7 between  $AIC_{TGM}$  and  $AIC_{TG}$  indicates an intermediate level of support for the simpler

model (Burnham, 2002). A conservative threshold of ( $AIC_{TGM}-AIC_{TG}$ ) in favor of TG (simpler) models is used to account for the retrieval and interpolation errors in the SMAP time series.

We use Ashman’s D (Ashman et al., 1994) as an independent test to quantify adequate separation of the modes of the fitted kernel densities of  $\theta_{RS}$ . We argue that a mere better fitting accuracy of TGM over TG models doesn’t indicate bimodality in  $\theta_{RS}$  density distribution. Popular derivations of Ashman’s D provide a dimensionless variable to quantify the separation of means of two heteroscedastic distributions of unequal standard deviation. However, mean and standard deviation may not be the representative estimates of the variability and central tendency of skewed distributions. Hence, a modified formulation of Ashman’s D is used in Eq. 3 as:

$$D = \frac{|MO_{dry} - MO_{wet}|}{\sqrt{\left(\frac{IQR_{dry}+IQR_{wet}}{2}\right)}} \quad (3)$$

where  $IQR_{dry}$  and  $IQR_{wet}$  are the interquartile ranges of  $p_{dry}$  and  $p_{wet}$  respectively. Following Ashman et al. (1994) and Vilasa et al. (2017),  $D > 2$  indicates adequate separation between the modes of  $p_{dry}$  and  $p_{wet}$  and hence, TGM model is selected as the appropriate model for  $\theta_{RS}$ .

### 3.3 Footprint-scale soil moisture drydown parameters

Assuming net lateral fluxes for a large ( $\sim 36$  KM) SMAP footprint to be negligible, soil water balance for a SMAP pixel of a uniform support ( $\sim 5$  cm) is given as:  $\Delta\theta_{RS}/\Delta t = P - ET - D$ , where P = precipitation, ET = evapotranspiration, and D = gravity drainage. Following a precipitation event, soil enters a period of drydown where any loss in  $\theta_{RS}$  can be attributed to ET and D. Hence, when P=0, the rate of SM loss between time  $t$  and  $t-1$ , i.e.  $[\Delta\theta_{RS}/\Delta t]$ , equals ET+D, where  $-\Delta\theta_{RS} = \theta_{RS}^t - \theta_{RS}^{t-1}$  (negative sign indicates net loss of SM), and  $\Delta t$  is the sampling frequency. The rate of SM loss,  $[\Delta\theta_{RS}/\Delta t]$ , decreases non-linearly with a decreasing  $\theta_{RS}^t$  (Laio et al., 2001; Rodriguez-Iturbe, 2000; Rodriguez-Iturbe et al., 1999). The relationship between  $\theta_{RS}^t$  and  $[\Delta\theta_{RS}/\Delta t]$  can be approximated as a piecewise-linear function called a SM drydown curve,  $\mathbf{L}(\theta_{RS})$ , as shown in Figure 1a. Theoretically,  $\mathbf{L}(\theta_{RS})$  consists of four hydrologic regimes, i.e., *i*) gravity-drainage (G), *ii*) energy-limited wet phase (W), *iii*) moisture-limited transitional phase (T), and *iv*) dry phase (D) in the order of decreasing  $\theta_{RS}$ . Parameters  $\theta^{GW}$ ,  $\theta^{WT}$  and  $\theta^{TD}$  represent the transition points between the consecutive hydrologic regimes and are assumed to be analogous to the field capacity, critical point (plant water stress threshold SM at the intersection of phase I and phase II ET) and wilting point respectively, as defined at the field scale. The rate of

SM losses in the gravity-drainage and transitional phase are given by  $m_1$  and  $m_2$  respectively. During the transitional phase of drydown, SM moderates the variance in ET through limiting control on the latent heat flux (Dirmeyer, 2011; Santanello et al., 2018). Hence,  $m_2$  represents the terrestrial component of the land-atmospheric coupling for the pixel. The constant-rate losses during wet ( $l_w$ ) and dry phase ( $l_d$ ) represent evapotranspiration loss at the potential rate, and soil evaporation due to vapor diffusion respectively.

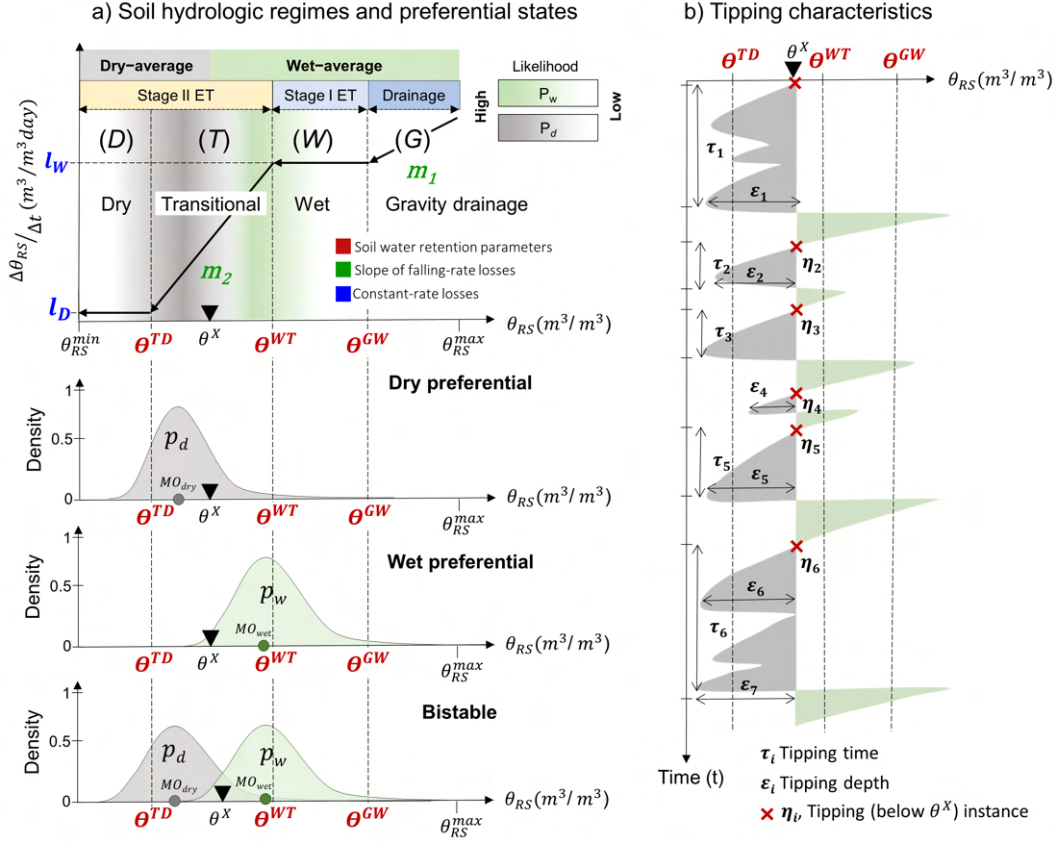


**Figure 1.** (a) A schematic representation of the piecewise  $\theta_{RS}$  drydown curve,  $L(\theta_{RS})$ , at remote sensing scale, overlaid with the density distribution of  $\theta_{RS}$  at dry-preferential, bistable and wet-preferential hydrologic states. The effective soil water retention parameters are, namely,  $\theta^{GW}$  (effective field capacity),  $\theta^{WT}$  (effective critical point) and  $\theta^{TD}$  (effective wilting point). The tipping point is shown as  $\theta^X$ . The green and gray shade in  $L(\theta_{RS})$  provides a schematic representation of the likelihood of the wet-average and dry-average density distribution of  $\theta_{RS}$  (b) A sample  $\theta_{RS}$  time series with tipping characteristics. The parameters,  $\theta^{GW}$ ,  $\theta^{WT}$ ,  $\theta^{TD}$  and  $\theta^X$  are estimated seasonally using  $\theta_{RS}$  observations for the respective months.

We use global seasonal estimates of  $L(\theta_{RS})$  parameters as given by Sehgal et al. (2021b). The best fitting parameters of  $L(\theta_{RS})$  are estimated from an ensemble of 300 models fitted on the seasonal SM drydown observations ( $[\theta_{RS}]$  v/s  $[\Delta\theta_{RS}/\Delta t]$ ) of five pathways – GW or {TD}, {W} or {D}, {WT}, {WTD}, and {T} using a least-squares approach with 10

x 30 cross validation and resampling. The mathematical formulation of these pathways is provided in Table S1 of the Supplementary material. Missing seasonal values for  $\theta^{TD}$  or  $\theta^{WT}$  for pixels with missed retrievals over long periods (for example, snow cover in high latitude regions) or dominance of partial drydown pathways, are gap-filled using the average values of the available seasonal estimates. In the case of the pixels following the drydown pathway T and TD, the value of  $\theta^{WT}$  is assumed to be the 1.05 times the maximum seasonal value of SM for the pixel following Sehgal et al. (2021a). For details on  $\theta_{RS}$  drydowns, readers are referred to Akbar et al. (2018), and Sehgal et al. (2021b).

### 3.4 Preferential hydrologic states and tipping characteristics of $\theta_{RS}$

The preferential state of  $\theta_{RS}$  represent the hydrologic conditions (dry, wet or both) most likely to sustain as a result of soil water balance and land-atmospheric feedbacks. The preferential hydrologic state of  $\theta_{RS}$  is identified based on the number of modes of the density distribution of  $\theta_{RS}$ , and the non-exceedance probability of  $\theta_{RS}$  above a threshold,  $\theta^X$ , given as  $P_{dry} = P(\theta_{RS} \leq \theta^X)$ . The threshold,  $\theta^X$ , is called the Tipping Point (in  $m^3/m^3$ ) and represents the intersection point between the wet- and dry-average conditions. When  $\theta_{RS} < \theta^X$ ,  $(L(\theta_{RS}) \in p_{dry}) > (L(\theta_{RS}) \in p_{wet})$ , and vice-versa. In the case of univariate TG models,  $\theta^X$  is assumed to be the arithmetic average of  $\theta^{TD}$  and  $\theta^{WT}$ . This assumption follows Sehgal et al. (2021a) where  $(\theta^{TD} + \theta^W)/2$  is used as the inflection point of the non-linear relationship between  $\theta_{RS}$  versus SM stress, further supported by a global scale analysis which shows a strong linear relationship between  $\theta^X$  and  $(\theta^{TD} + \theta^W)/2$  for pixels with bivariate  $\theta_{RS}$  density distribution (Figure S3 of the Supplementary material). Recall from Section 3.1,  $K=1, 2$  for unimodal and bimodal densities respectively, then three hydrologic states of  $\theta_{RS}$  are defined (Eq. 4) as:

$$Hydrologic - State = \begin{cases} \text{Dry - preferential,} & K = 1; P(\theta_{RS} \leq \theta^X) > 0.5 \\ \text{Bistable,} & K = 2 \\ \text{Wet - preferential,} & K = 1; P(\theta_{RS} \leq \theta^X) < 0.5 \end{cases} \quad (4)$$

For a given  $\theta^X$ , we define three tipping characteristics to capture the intensity, duration, and frequency of the excursion of  $\theta_{RS}$  into a dry-average conditions ( $\theta_{RS} \leq \theta^X$ ) as *i*) Mean Tipping Depth,  $\bar{\varepsilon}$ , *ii*) Mean Tipped Time,  $(\bar{\tau})$ , and *iii*) Tipping Count,  $\eta$  as shown in Figure 1b. Let's assume  $\varepsilon_i$  represents the maximum absolute deviation between  $\theta_{RS}$  from  $\theta^X$ , divided by  $\theta^X$  during a dry-tipping (shift from wet- to dry-average conditions) event, *i*. Then the mean tipping depth,  $\bar{\varepsilon} [-]$  is given by Eq. 5 as:

$$\bar{\varepsilon} = \frac{\sum_{i=1}^{\eta} \varepsilon_i}{\eta} \quad (5)$$

Hence,  $\bar{\varepsilon}$  is the average maximum deviation of  $\theta_{RS}$  relative to  $\theta^X$ . Tipping Count,  $\eta$  is defined as the total count of dry-tipping of  $\theta_{RS}$  from a wet-average to dry-average conditions. During each dry-tipping event,  $i$ , the duration of  $\theta_{RS} < \theta^X$  i.e.,  $\tau_i$ , is governed by the noise-induced perturbations in precipitation, which follows a marked Poisson process with exponentially distributed interarrival time. Hence, the density distribution of  $\tau_i$  follows a positively skewed density distribution which can be modeled with an exponential curve (Eq. 6) of the form:

$$P(\tau) = \gamma \cdot e^{(-\gamma \cdot \tau)} \quad (6)$$

where,  $\gamma$  is the rate parameter of the exponential curve. The Mean Tipped Time, ( $\bar{\tau}$ ) [days], is estimated by Eq. 7 as:

$$\bar{\tau} = \frac{1}{\gamma} \quad (7)$$

Previously, Tamea et al. (2011), have demonstrated the application of double exponential, pareto and exponential functions in modeling the density distribution of  $\tau$ . In this study, univariate exponential decay model is used to model  $\tau$  due to parsimonious parameterization and satisfactory performance at a global scale. To minimize the impact of the limited number of seasonal observations of the dry-tipping events, the dataset for curve fitting is obtained from the histogram of  $\tau$  with the size of the bins fixed to  $\max(\eta/2, 10)$  to ensure sufficient data samples within each bin.

### 3.5 Partitioning of intra-biome ecoregions using $\theta_{RS}$ tipping characteristics

We use Non-linear principal component analysis, NLPCA, (Kramer, 1991; Scholz et al., 2005) to reduce the dimensionality of the seasonal  $\theta_{RS}$  tipping characteristics, and obtain a single global spatial field of independent, uncorrelated feature of the estimates. Three indices, Separation Ratio ( $R_{Sep}$ ), Separation Distance ( $d_{Sep}$ ) and Separation Score ( $S_{Sep}$ ) are then defined to characterize the difference in mean NLPC of a pair of regions ( $i, j$ ), with  $i \neq j$ , using Tukey-Kramer (a modification of Tukey's test for unequal sample sizes, Dunn (1961); Rafter et al. (2002)) and Bonferroni (Bland & Altman, 1995) tests.

### 3.5.1 Non-linear principal component analysis of $\theta_{RS}$ tipping characteristics

NLPCA is an unsupervised, non-linear generalization of standard principal component analysis (Diamantaras & Kung, 1996), which uses artificial neural networks (ANN)-based, multilayer perceptron autoencoder to perform an identity mapping between the input  $I$  and the output  $O$  features. Due to reliance on a non-linear ANN framework, NLPCA provides advantage over standard (linear) PCA by capturing complex features of the inputs, and displays less sensitivity to noise (Monahan, 2000). The input is approximated by iteratively passing the output through the network and minimizing the squared reconstruction error  $E = \|O - I\|^2$ . The network consists of two parts, *i*) the extraction function ( $\Omega_{extr}: I \rightarrow Z$ ), and *ii*) the inversion function ( $\Omega_{inv}: Z \rightarrow O$ ). Each part consists of a hidden layer which facilitates non-linear mapping within the network. The layer  $Z$  is called a bottleneck, i.e., a layer of fewer nodes than at input, where the data is projected into a lower dimensional space. The inverse model ( $\Omega_{inv}: Z \rightarrow O$ ) extracts the required components by only modelling the inversion function of the auto-associative network, and thus, is computationally efficiency over training both parts. The output  $O$  depends on the input  $Z$ , and the network weights in the hidden and the output layers. The errors are minimized by conjugate gradient descent algorithm (Nazareth, 2009), wherein the partial errors are iteratively propagated back to the input layer.

NLPCA uses a missing data estimation approach for validation of the ANN, where one or more elements of the input sample are randomly eliminated from model training. The mean of the squared errors between the randomly removed values and their NLPCA estimations is used as the generalization error (Scholz, 2012). Due to the robustness of NLPCA in capturing high-order complexity in natural processes, it is used in diverse hydrological applications, such as, catchment regionalization (Razavi & Coulibaly, 2013, 2016), missing data imputation in climate variables (Abdelkader & Yerdelen, 2022; Miró et al., 2017), watershed discretization (Sardooi et al., 2019). We use 5000 iterations of the network with non-linear ‘*tanh*’ activation function to reduce the dimension of the seasonal means  $\theta_{RS}$  tipping characteristics to a single non-linear principal component (NLPC), which captures 97.4% variability in the input features. NLPC is normalized to a range  $\in [0,1]$  to match the theoretical range of  $\theta_{RS}$ . For more details on NLPCA, the readers are referred to Scholz (2012), Scholz et al. (2005) and Scholz et al. (2008).

### 3.5.2 Statistical test for differences between mean inter-ecoregion tipping characteristic

Tukey-Kramer and Bonferroni are post-hoc tests for the pairwise comparison of means with the null hypothesis of  $H_o : \mu_i = \mu_j$ , where  $\mu_i$  and  $\mu_j$  are the mean observations for the groups  $i$  and  $j$  respectively (in this study, ecoregions or biomes). If  $\frac{N}{2}C$  represents the total (unique) combinations of the groups,  $n^*$  indicate the subset of  $\frac{N}{2}C$  with statistically significant difference in inter-group NLPC ( $p$ -value  $> 0.05$ ), and  $d$  is the difference in the mean NLPC for groups  $i$  and  $j$ , when  $(i,j) \in n^*$ , then  $R_{Sep}$  and  $d_{Sep}$  are given by Eq. 8-9

$$d_{Sep} = \sum_{i=1}^{n^*} d/n^* \quad (8)$$

$$R_{Sep} = \frac{n^*}{\frac{N}{2}C} \quad (9)$$

The two indices,  $R_{Sep}$  and  $d_{Sep}$  are combined to generate a Separation Score ( $S_{Sep}$ ) given by Eq.10:

$$S_{Sep} = \sqrt{d_{Sep}^2 \cdot R_{Sep}^2} \quad (10)$$

Indices  $d_{Sep}$ ,  $R_{Sep}$ , and  $S_{Sep}$  have a range of (0,1). Higher values of  $d_{Sep}$  or  $R_{Sep}$  indicate that a larger difference in the mean inter-region NLPC, or a higher number of regional pairs have statistically significant difference in NLPC means, respectively. Bonferroni method uses thresholds based on the t-distribution and is more conservative than the Tukey test, that tolerates type I errors and uses studentized range distribution (S. Lee & Lee, 2018; Ruxton & Beauchamp, 2008). Hence, we use both tests to provide a balance between statistical power and conservatism in the evaluation of the results. To ensure sufficient samples for the statistical tests, only regions with more than 100 observations are included in the analysis. The analysis is carried out at two scales: biomes (comparing NLPC within biomes) and ecoregions (comparing NLPC of ecoregions nested within respective biomes).

## 4 Results and discussion

### 4.1 Preferential hydrologic states of $\theta_{RS}$ for sample pixels in contrasting climates

The impact of scaling and observational challenges on identifying various soil hydrologic regimes at RS-footprint scale is illustrated in Figure 2, where the fitted  $\theta_{RS}$  density distribution of  $\theta_{RS}$  with overlaid  $L(\theta_{RS})$  is shown for three sample pixels in arid, semi-arid and humid climate. For the arid and semi-arid pixels, the density distribution of unimodal  $\theta_{RS}$  is heavily right-skewed with the mode close to the low ends of the transitional regime.

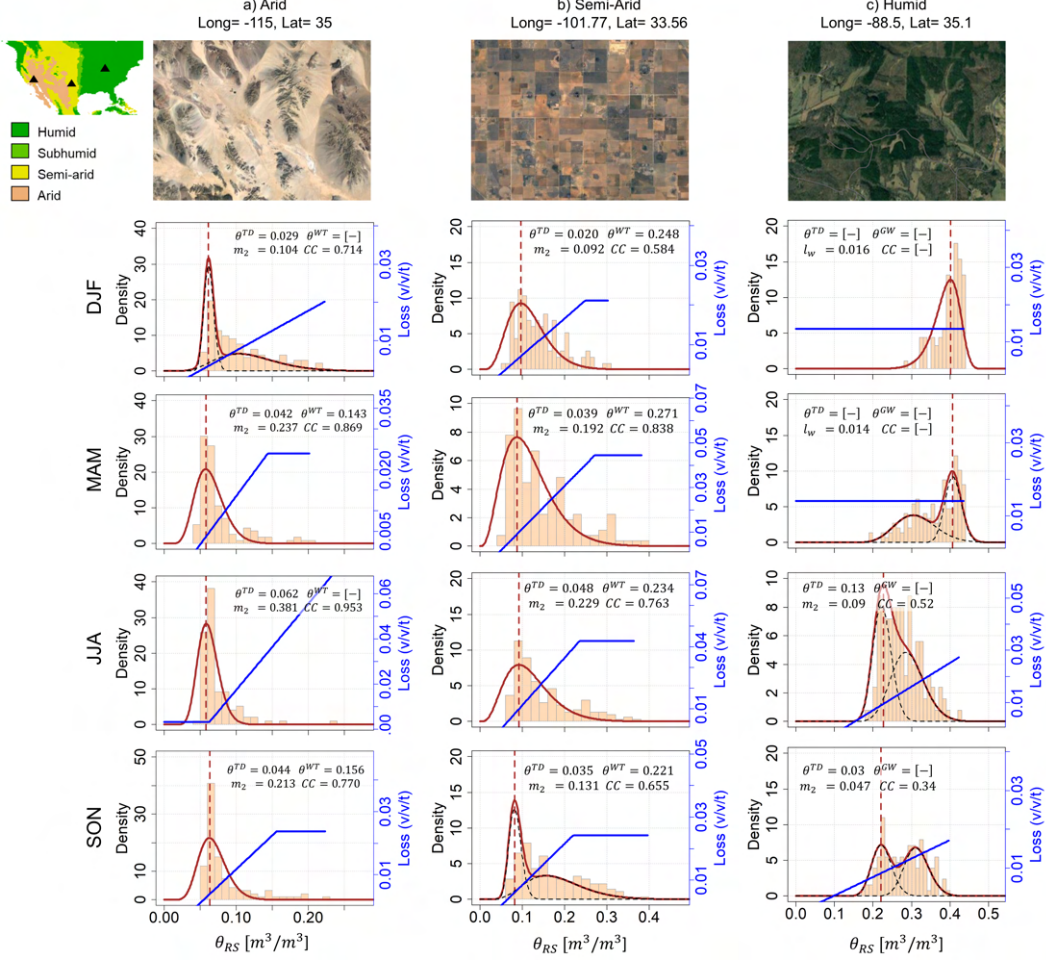


**Figure 2.** Seasonwise fitted density distributions (brown) and drydown curves (blue line,  $[\theta_{RS}]$  v/s  $[\Delta\theta_{RS}/\Delta t]$ ) for sample pixels from **a)** Arid (Essex, California), **b)** Semi-Arid (Lubbock, Texas) and **c)** Humid (Selmer, Tennessee) climate. The spatial panels on the top provide an overview of the landscape in the SMAP footprint (Courtesy: Google Earth). The inset on the top left shows the geographic location of the selected pixels. The values of the drydown parameters and the respective goodness of fit ( $CC$ = correlation coefficient) is provides as a text within the plot.

Observations of  $\theta_{RS}$  shortly after storm events are recorded as a distinct node in the  $\theta_{RS}$  density distribution, causing  $\theta_{RS}$  bimodality in arid/semi-arid pixel during DJF/SON and over most seasons for the humid pixel. To account for the heterogeneous vegetation characteristics and  $\theta_{RS}$  distribution due to variable precipitation or irrigation patterns within the RS-footprint, simpler pathways of  $L(\theta_{RS})$  are preferred over more complicated forms in the fitting algorithm to minimize parameteric uncertainty and prevent overfitting (Sehgal et al., 2021b). In these cases, wet-average conditions are recorded as a distinct node within the moisture-limited (transitional) regime, albeit on the wetter edge of the transitional regime, for example, in the arid pixel during DJF, semi-arid pixel during SON, and for the humid

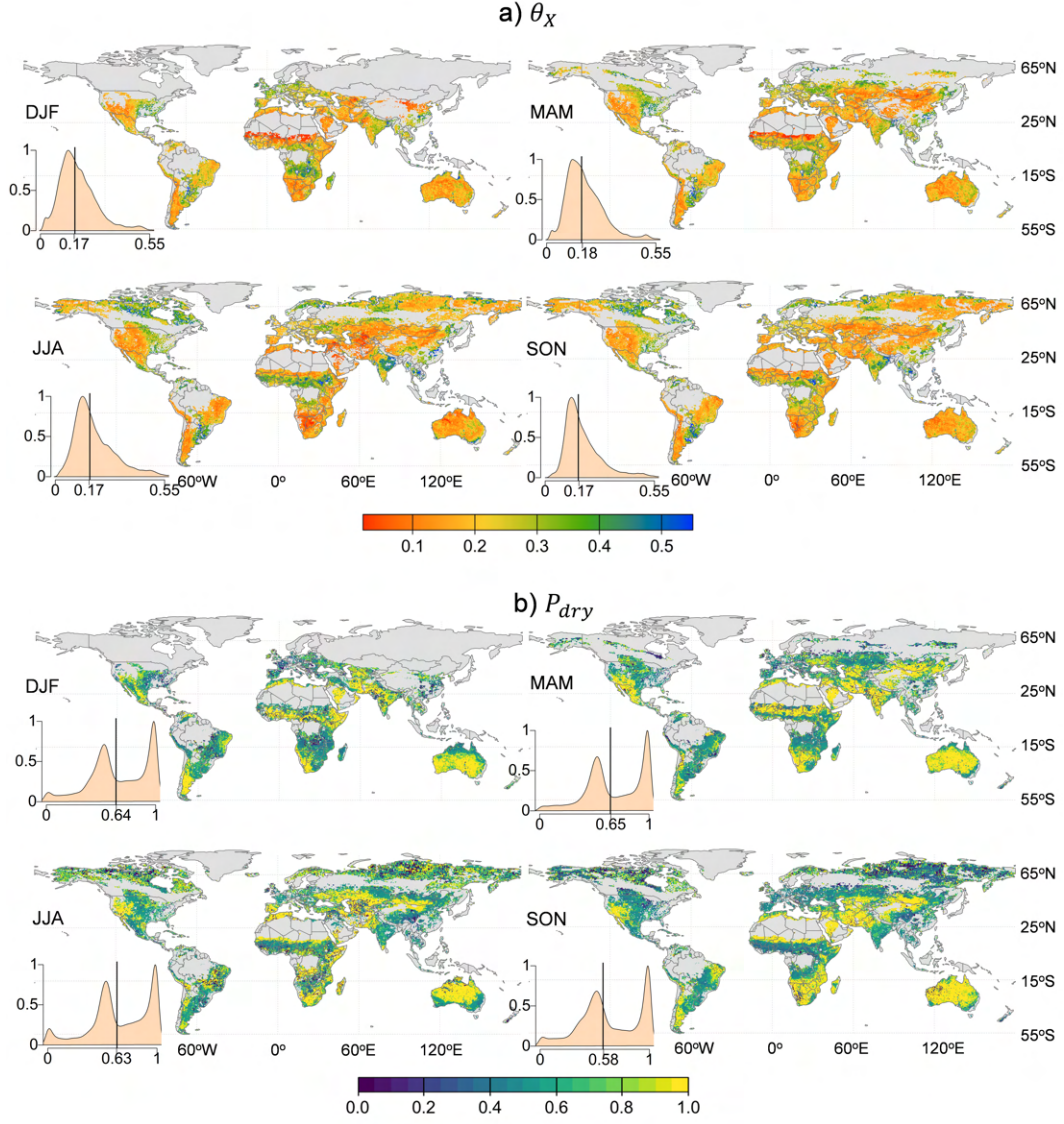


**Figure 3.** Seasonal global spatial distribution of **a)**  $\theta^X$  and **b)**  $P_{dry}$ , given as  $P(\theta_{RS} \leq \theta^X)$ . The inset shows the density distribution of the estimates for the respective season. Vertical black lines in the density distribution indicates the median value. Gray color in the plots with missing data/estimates.

pixel during JJA and SON. In the case of the humid pixel, drydown curve of the form  $\{W\}$  is proposed to capture the energy-limited conditions during both DJF and MAM seasons, which ignores the dry-average conditions during MAM. This can partially be attributed to increased SMAP retrieval errors in growing season, which contributed to increased uncertainty in identifying energy-limited regimes of  $\theta_{RS}$  drydowns. Alternatively, while multiple hydrologic regimes may be identified with the help of drydown curves, soil may predominantly exhibit preference for a certain state, with low probability of sustenance of other

hydrologic regimes at a seasonal scale. Hence, while drydown curves provide critical SM thresholds of SVC interactions, temporal sustenance of key ecohydrological processes at seasonal scale is determined by the most preferred hydrological state of SM— an information missing from the drydown curves.

#### 4.1.1 Preferential hydrologic states of global $\theta_{RS}$

Global seasonal estimates of  $\theta^X$  and  $P_{dry}$  are shown in Figure 3. As observed,  $\theta^X$  show a positive skew with the median values between 0.17-0.18  $m^3/m^3$ . Except for the regions with bimodal distribution,  $\theta^X$  is derived as the arithmetic mean of  $\theta^{WT}$  and  $\theta^{TD}$ . The seasonal variability in  $\theta^X$  is driven largely by the climatic controls on  $\theta^{WT}$  through the changes in land-surface characteristics like subgrid-scale  $\theta_{RS}$  distribution and vegetation patterns. The effective wilting point,  $\theta^{TD}$ , shows a low temporal variability (for details, refer to Figure S4 of the Supplementary material) due to low moisture conditions. Hydroclimate exerts a strong control over the global spatial distribution of  $P_{dry}$ . Arid regions show a markedly high  $P_{dry}$  (0.96 [-]), attributed to long dry periods with low and infrequent precipitation, compared to semi-arid, sub-humid and humid hydroclimates ( $P_{dry} = 0.57, 0.55$  and  $0.54$  [-] respectively). The global density distribution of  $P_{dry}$  shows two distinct nodes, one between 0.52-0.53 [-] and another at  $\sim 0.985$ [-], with the seasonal global median values between 0.58-0.64 [-]. A smaller number of pixels in high latitudes show low  $P_{dry}$  as the soil sustains wet-average conditions in these regions. Importantly, seasonal climatic variability drastically alters the regional distribution of  $P_{dry}$ , as seen prominently seen over global monsoonal regions. Monsoonal precipitation in boreal summer and fall dramatically reduces  $P_{dry}$  over India and Mexico. Similarly, tropical, and sub-tropical regions of Australia, the Iberian Peninsula, Sahel and South-eastern part of the African continent, among others, show large changes in  $P_{dry}$  values over the seasons.

We recall that the preferential hydrologic states are classified based on the number of modes of  $\theta_{RS}$  density distribution and  $P_{dry}$  following Eq. 4. The spatial distribution of the seasonal preferential hydrologic states of  $\theta_{RS}$  is shown in Figure 4. Dry preferential states are predominant in arid hydroclimate accounting for 62% (average) global arid pixels with  $\pm 9\%$  variability across the seasons. Semi-arid and sub-humid climates show bistable preferential states accounting for, respectively,  $28 \pm 11\%$  and  $17 \pm 8\%$  pixels. Wet preferential states are observed over a small fraction of global pixels accounting for 6-9% of humid, sub-humid and semi-arid climates and  $\sim 4\%$  in arid regions. The prevalence of wet-preferential states in humid hydroclimates, however, may actually be higher than that reported here due to missed retrievals over heavily vegetated pixels in humid regions. Hydroclimate-wise summary of

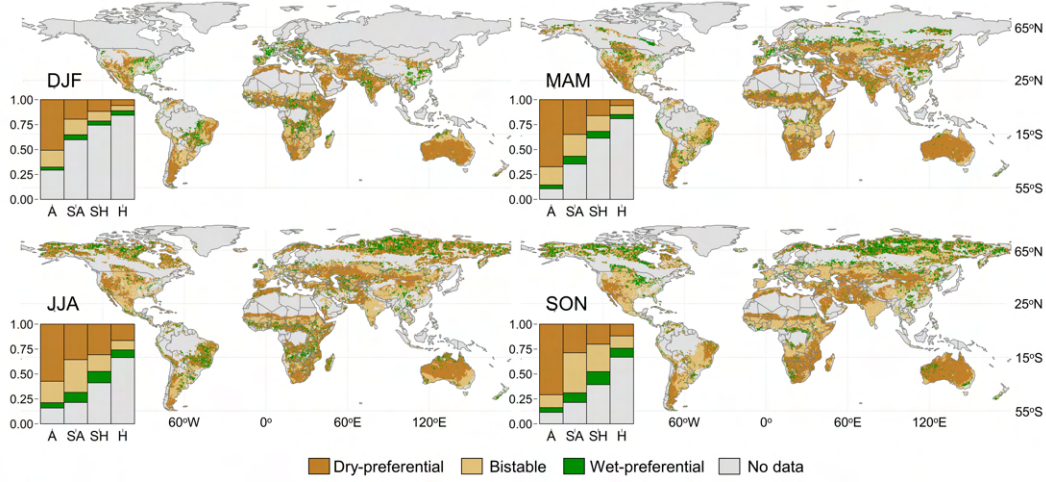


**Figure 4.** Seasonal global spatial distribution of the preferential hydrological states of  $\theta_{RS}$ . The inset shows climate-wise fractional global coverage of each preferential state for the respective season. Gray color in the plots with missing data or estimates.

fractional global cover of each preferential hydrologic states is provided in Table S2 of the Supplementary material.

## 4.2 Bistability in $\theta_{RS}$ states

Bimodality in the hydrologic states of  $\theta_{RS}$  implies two stable states in the density distribution of  $\theta_{RS}$  corresponding to  $MO_{dry}$  and  $MO_{wet}$ . As observed in Figure 5a-b,  $MO_{dry}$  is observed predominantly within the moisture-limited regime (second quadrant,  $\theta^{TD} \leq MO_{dry} \leq \theta^{WT}$ ). The likelihood of  $MO_{dry}$  is highest as  $\theta_{RS}$  approaches  $\theta^{TD}$  due to increasing soil matric potential with a decrease in  $\theta_{RS}$  during drydown. In contrast,  $MO_{wet}$  can be observed in first and second quadrants i.e., when  $MO_{wet} \leq \theta^{WT} \leq \theta^{GW}$  (moisture-limited regime) or when  $\theta^{WT} \leq MO_{wet} \leq \theta^{GW}$  (energy-limited regime) respectively. Wet and gravity drainage regimes are transient hydrologic regimes primarily controlled by leakage and evaporative losses at the potential rates. Hence, the kernel density of  $MO_{wet}$  is observed to peak close to  $\theta^{WT}$ , as the soil begins to transition from wet to transitional regime. Both  $MO_{dry}$  and  $MO_{wet}$  show strong influence of soil texture, which regulates the soil's impedance to moisture loss under drydowns. Hence, increase in the pixel clay content corresponds with an increase in  $MO_{dry}$  and  $MO_{wet}$  as shown in Figure 5c-d. In soils with high clay content (>40%), shrinking and swelling may cause temporal variability in the observed seasonal values of  $MO_{dry}$ . Seasonal global estimates of  $MO_{dry}$  and  $MO_{wet}$  are show in Figure S5 of the Supplementary material. As discussed, Figure 5a-b place an emphasis on the importance of critical point ( $\theta^{WT}$ ) as an important threshold of  $\theta_{RS}$  dynamics, as opposed to field capacity ( $\theta^{GW}$ ) at RS-footprint scale due to better observability

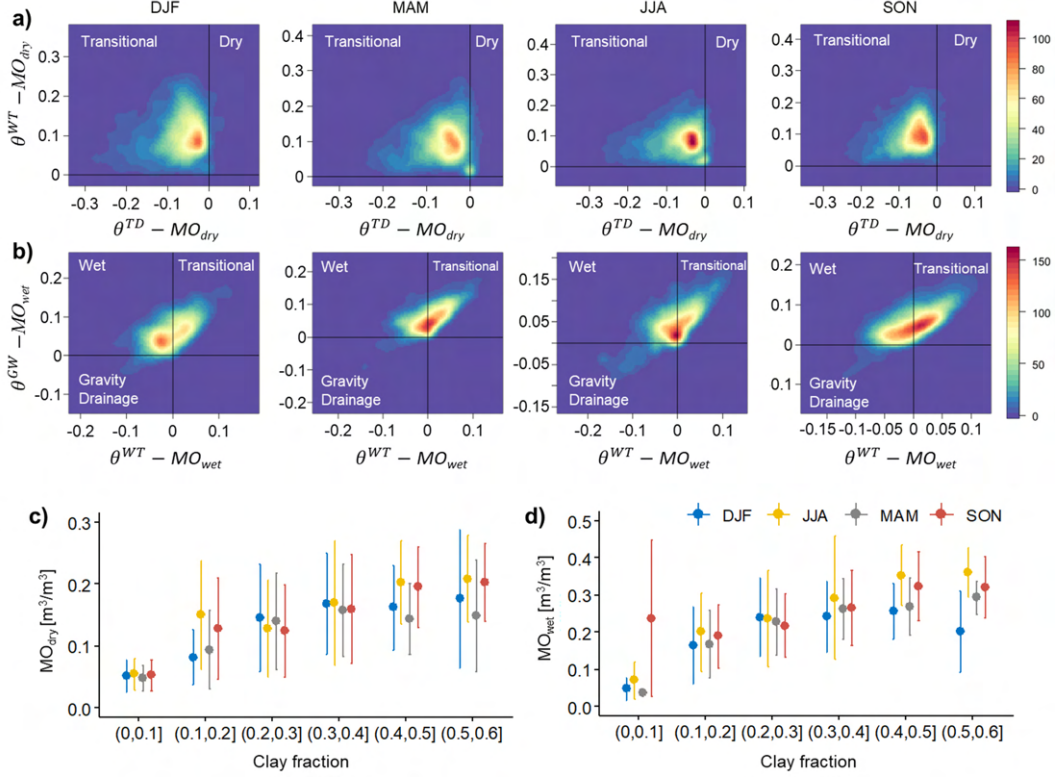


**Figure 5.** Scatter plots of the a) difference between  $\theta^{TD}$  and  $MO_{dry}$  ( $\theta^{TD}-MO_{dry}$ ) versus the difference between  $\theta^{WT}$  and  $MO_{dry}$  ( $\theta^{WT}-MO_{dry}$ ) b) difference between  $\theta^{WT}$  and  $MO_{wet}$  ( $\theta^{WT}-MO_{wet}$ ) versus the difference between  $\theta^{GW}$  and  $MO_{wet}$  ( $\theta^{GW}-MO_{wet}$ ). The stable states of  $\theta_{RS}$ , given by  $MO_{dry}$  and  $MO_{wet}$ , are mapped to corresponding hydrologic regimes (as labeled in white) based on the deviation from the SWRPs ( $\theta^{TD}$ ,  $\theta^{WT}$ , and  $\theta^{GW}$ ). Only pixels with bimodal  $\theta_{RS}$  density distribution are used in this analysis. c)– d) Season-wise summary of  $MO_{dry}$  and  $MO_{wet}$  with clay fraction. The circular dot represents the group-wise median estimates, while the error bars indicate the inter-quantile range of the values.

and closer relevance to the wet-average SM state. Several recent studies have highlighted the importance of critical soil moisture in terrestrial energy and water flux partitioning (Fu et al., 2022; Schwingshackl et al., 2017), however, dependency of classical soil hydrology on field capacity may warrant revisiting for better applicability across spatial scales.

### 4.3 Ecohydrological linkages of the $\theta_{RS}$ preferential hydrologic states

Figures 4 and 5 help affiliate the spatiotemporal manifestation and variability of preferential  $\theta_{RS}$  states to the dominant hydrological processes. Dry-preferential state indicate the prevalence of moisture-limited conditions over the RS-footprint, when  $\theta_{RS}$  exerts a limiting control over the temporal variability in ET. A decrease in  $\theta_{RS}$  causes reduced evaporative cooling of the land-surface and may initiate a positive SM-precipitation feedback (Lei et

al., 2018; Zeppetello et al., 2019). As  $\theta_{RS}$  shifts farther below  $\theta^X$ , the ratio of sensible- to latent heat flux increases. This accentuates further drying of soil and decreases the moist static energy (i.e., low-level moisture) in the atmospheric boundary layer, which reduces the likelihood of precipitation (Alessi et al., 2022). Wet-preferential state, on the contrary, indicate prevalence of a “*climate-controlled*” state where primarily mechanism of  $\theta_{RS}$  loss is gravity drainage or ET at potential/ near-potential rates, limited by the radiative fluxes (Seneviratne et al., 2010). Such conditions may lead to a negative SM-precipitation feedback. A shift in  $\theta_{RS}$  farther above  $\theta^X$  correspond to lower sensible heat which reduces the near-surface temperatures and impedes the development of convective precipitation through lowering of the atmospheric boundary layer (Taylor et al., 2012). Previously, Tuttle and Salvucci (2016) reported contrasting linkages between SM and precipitation over western (positive feedback) and eastern (negative feedback) U.S. which correspond, respectively, with regions predominantly displaying dry-preferential and wet-preferential hydrologic states.

Bistable state indicates a dynamic coexistence of complimentary (both positive and negative) SM-precipitation feedback processes as explained for the dry- and wet-preferential states. The wet-average density of the bimodal  $\theta^X$  distribution correspond to the  $\theta_{RS}$  during energy-limited hydrologic regimes (negative SM-precipitation feedback). The dry-average density, on the other hand, relate to the moisture-limited hydrologic regimes – dry or transitional, dominated by positive SM-precipitation feedback. Bistable states exist in regions where the climatic conditions are conducive of facilitating the dynamic shift of SM states through strong SM-precipitation feedback processes (Yin et al., 2014). Such conditions are observed in the semi-arid and subhumid climates characterized by sufficient availability of both SM and energy to ensure mesoscale terrestrial controls on ET variability at the sub-seasonal timescale. Such regions have been characterized as the “*hotspots*” of SM-precipitation coupling (Koster et al., 2004). Additionally, the bistable  $\theta_{RS}$  states are observed over global monsoonal regions such as: India, Sahel, Mexico and US South-west during boreal summer/fall, and boreal winter and spring in Southern Brazil, South-central Africa, and Northern Australia. Hydroclimatic conditions in these regions can facilitate sub-seasonal coexistence of dry and wet-preferential states though land-surface controls over convective precipitation. Mesoscale monsoonal storms create a heterogeneous  $\theta_{RS}$  distribution, which helps create temperature and humidity gradients in the planetary boundary layer (Barton et al., 2019; Gantner & Kalthoff, 2009), especially under sparse vegetation condition (Gallego-Elvira et al., 2016). This favors convective initiation (Lohou et al., 2014), and a shift in the  $\theta_{RS}$  state to wet-average conditions. Precipitation recycling observed over the monsoonal regions of Mexico and U.S. South-west (Dominguez et al., 2008), India (Kumar et al., 2021; Pathak et al., 2014; Sujith et al., 2017), Sahel (Yu et al., 2017), Tibetan plateau (Kurita & Yamada, 2008) may further enhance bistability in  $\theta_{RS}$  state.

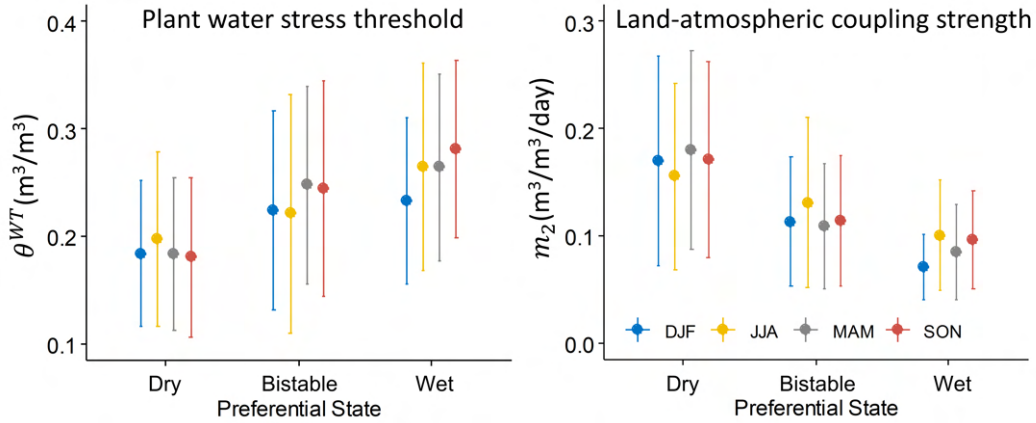


**Figure 6.** Summary of plant water stress threshold, given by critical point,  $\theta^{WT}$ , and land-atmospheric coupling strength ( $m_2$ ) summarized for the preferential soil hydrologic states.

Unsurprisingly, the preferential soil hydrologic states can exert a strong ecohydrological control on the SVC dynamics through linkages with the critical thresholds of plant water stress (given by the critical point,  $\theta^{WT}$ ) and land-atmospheric coupling strength ( $m_2$ ) as Figure 6 demonstrates. A shift in the preferential  $\theta_{RS}$  state from dry to wet is associated with a decrease in the value of  $m_2$ . Wet-preferential states are characterized by a decreasing control of  $\theta_{RS}$  over the variability in ET, and hence, weaker land-atmospheric coupling, in line with the findings of McColl et al. (2017). On the other hand, the critical threshold of plant water stress decreases significantly from regions with wet-preferential to dry-preferential  $\theta_{RS}$ , and is characterized with coexistence of coarse textured soils, and plant species with drought resilient adaptations (Fu et al., 2022, 2021).

**Table 1.** Median estimates (and standard deviation) of the tipping characteristics for preferential soil hydrologic states.

| Hydrologic state | $\bar{\epsilon}$ [-] | $\bar{\tau}$ [days] | $\eta$ [-] |
|------------------|----------------------|---------------------|------------|
| Dry-preferential | 1.38(0.20)           | 5.43(2.87)          | 19(9.99)   |
| Bistable         | 1.25(0.12)           | 3.67(1.89)          | 25(11.76)  |
| Wet-preferential | 1.13(0.09)           | 3.08(0.98)          | 22(10.93)  |

#### 4.4 Spatiotemporal variability and controls of global $\theta_{RS}$ tipping characteristics

Global seasonal estimates of the three tipping characteristics are shown in Figure 7. Seasonal estimates of  $\bar{\epsilon}$  follow a skewed distribution with seasonal median values ranging between 3.56-4.72 [-]. Similarly, global median estimates of  $\eta$  and  $\bar{\tau}$  follow a range of 17-

28 [days] and 1.24-1.32 [-] respectively. Global drylands have characteristically long dry periods with scarce (if any) intermittent precipitation. This may reduce the goodness-of-fit of the exponential distribution by shifting the density of  $\tau$  to larger values in arid climates. Overall, the fitting accuracy of the exponential curve on the distribution of  $\tau$  is found to be satisfactory based on high  $R^2$  globally and three select pixels as shown in Figures S6-7 of the Supplementary material. The respective median values of the tipping characteristics for each preferential hydrologic state are summarized in Table 1 to illustrate the characteristic properties of each preferential  $\theta_{RS}$  hydrologic state. Expectedly, dry-preferential states are characterized by high  $\bar{\varepsilon}$  and  $\bar{\tau}$  (1.38 [-] and 5.43 [days] respectively), and consequently, lowest values of  $\eta$  among other preferential states of  $\theta_{RS}$ . In contrast the wet preferential states are characterized by short ( $\bar{\tau}$  with a global median of 3.08 [days]) and low intensity ( $\bar{\varepsilon}$  with a global median of 1.13 [-]) excursions into the dry-average conditions. Pixels with bistable preferential state show a combination of a high rate of dry-average down-tipping ( $\eta = 25$  [-]), albeit, of intermediate duration ( $\bar{\tau} = 3.67$  [days]) and intensity ( $\bar{\varepsilon} = 1.25$  [-]). A summary of seasonal tipping characteristics for different hydroclimates and soil texture (clay content) is given in Figure 8.

#### 4.5 Ecosystem linkages of $\theta_{RS}$ tipping characteristics

Preferential hydrologic states are the physical manifestation of the tipping characteristics, which, as discussed previously, are controlled by the spatiotemporal variability in precipitation characteristics, and the non-linear controls of soil texture and vegetation on the rate of drydowns and critical thresholds of SVC interactions. The intensity, duration and frequency of SM transition into dry-average conditions determines the impact on vegetation and patterns of recovery from intense water stress (Rodríguez-Iturbe & Porporato, 2007). An increase in aridity and a decreasing clay content overlaps with an increase in  $\bar{\varepsilon}$  and  $\bar{\tau}$ . This indicates a mutually inclusive control of climate, soil texture on  $\theta_{RS}$  tipping characteristics and vegetation characteristics.

Figure 9 shows a ternary representation of the normalized mean seasonal tipping characteristics with dominant plant function types, climate and soil texture. The pixels with a unique combination of plant function types, climate and soil texture occupy a distinct region in the  $\bar{\varepsilon} - \eta - \bar{\tau}$  ternary space, indicating that  $\theta_{RS}$  tipping characteristics are linked to the coexistence of unique soil, vegetation and climatic conditions at a regional scale. This assumption is supported by Figure 10a, where an RGB composite of normalized mean seasonal estimates of the  $\theta_{RS}$  tipping characteristics is observed to closely follow the spatial patterns partitions within global biomes. A comparison of inter-biome mean NLPC using Tukey-Kramer and Bonferroni test demonstrates high skill in partitioning global biomes with

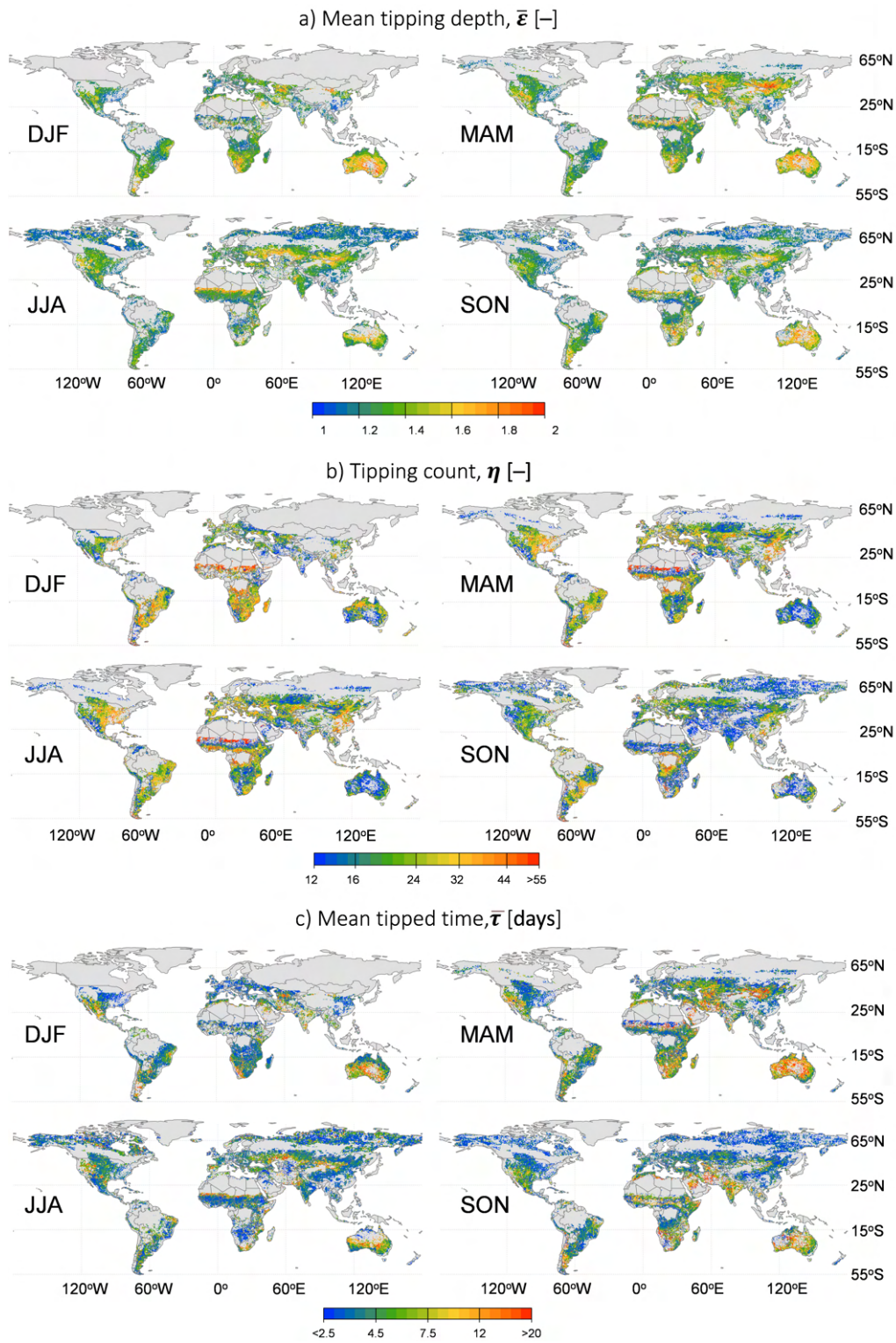


**Figure 7.** Global seasonal estimates of *a*) Mean tipping depth,  $\bar{\epsilon}$  [-], *b*) Tipping count,  $\eta$  [-] and *c*) Mean tipped time,  $(\bar{\tau})$  [days]. The colors are mapped at a logarithmic scale for a better contrast between divergent values.

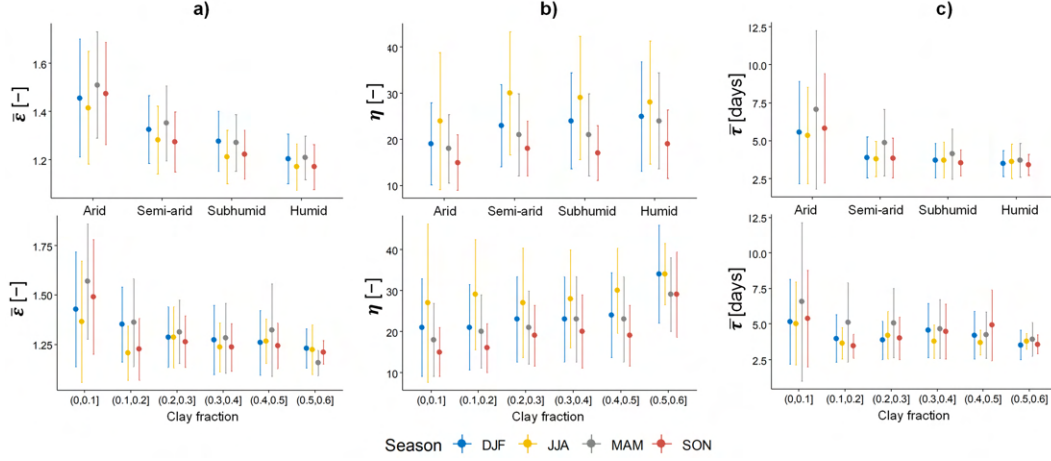


**Figure 8.** Summary of global seasonal estimates of **a)** Mean tipping depth,  $\bar{\varepsilon}$  [-], **b)** Tipping count,  $\eta$  [-] and **c)** Mean tipped time,  $(\bar{\tau})$  [days] based on (*top*) hydroclimates and (*bottom*) pixel clay fraction. The solid dots in the plots represent class-wise median values, while the error bars provide the interquartile range of the estimates.

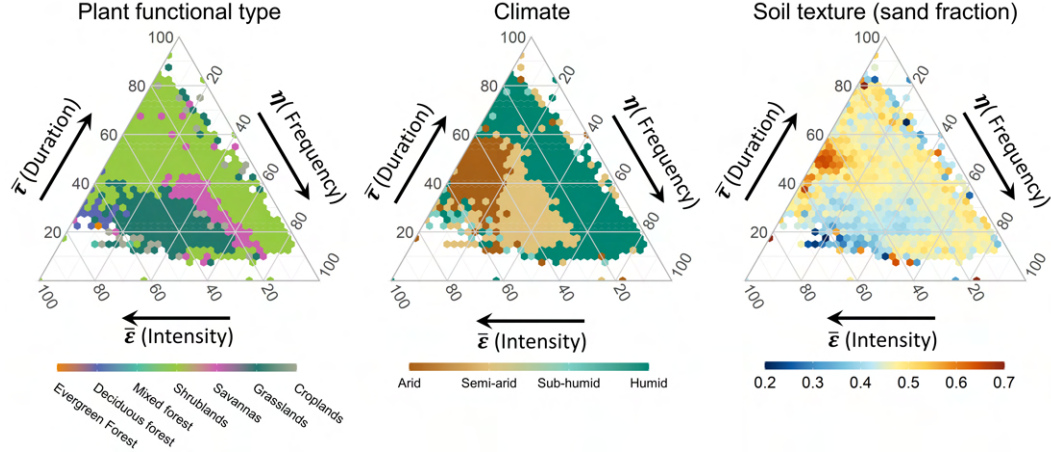


**Figure 9.** Ternary ( $\bar{\varepsilon} - \eta - \bar{\tau}$ ) representation of **a)** Sampling density of the seasonal mean  $\theta_{RS}$  tipping characteristics with **b)** dominant plant functional type, **c)** climate and **d)** soil texture (sand fraction). The values for the variables increase in the clockwise direction. The seasonal tipping characteristics are averaged prior to normalization to a scale of 0-100 using global minima and maxima.

$R_{Sep}$  of 0.89 and 0.91;  $d_{Sep}$  of 0.59 and 0.54; and  $S_{Sep}$  of 0.73 and 0.70, respectively (Figure 10b). Biome-wise summary of the NLPC of the  $\theta_{RS}$  tipping characteristics is provided in Figure 10c. The control of soil texture on  $\theta_{RS}$  tipping characteristics is conditional upon the length of the drydown and exerts a second-order influence on  $\bar{\varepsilon}$  and  $\bar{\tau}$ . Fine textured soils exhibit a smaller  $\bar{\varepsilon}$  compared to sandy soils due to higher capillary potential preventing the loss of  $\theta_{RS}$ . Soil texture exerts a stronger control over the deterministic dynamics of  $\theta_{RS}$ , prominently during late transitional or dry hydrologic states (Sehgal et al., 2021b). Longer

drydowns are favored by extended inter-storm periods typical to arid hydroclimates, where a combination of sandy soils and scant precipitation lead to high values of  $\bar{\varepsilon}$  and  $\bar{\tau}$ , and low values of  $\eta$ . This favors the “*inverse texture effect*” for coarse texture soils in arid/semi-arid climates as observed by Fernandez-Illescas et al. (2001). In regions with high seasonal  $\bar{\varepsilon}$  and  $\bar{\tau}$ , the surface soil layer decouples from the rootzone, preventing excessive rootzone moisture loss. This facilitates continued moisture availability to local vegetation from the deeper soil layers.

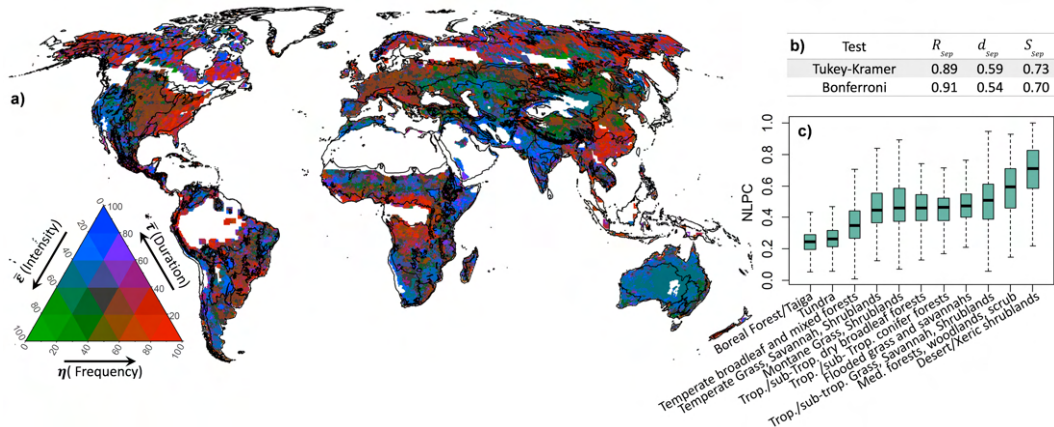


**Figure 10.** *a*) Global ternary (Red–green–blue) color composite of mean seasonal tipping characteristics with overlapping boundaries of global biomes, *b*) Values of Separation fraction ( $R_{Sep}$ ), Separation distance ( $d_{Sep}$ ) and Separation score ( $S_{Sep}$ ) using Tukey-Kramer and Bonferroni tests for inter-biome separation of NLPC means *c*) Summary of NLPC for global biomes.

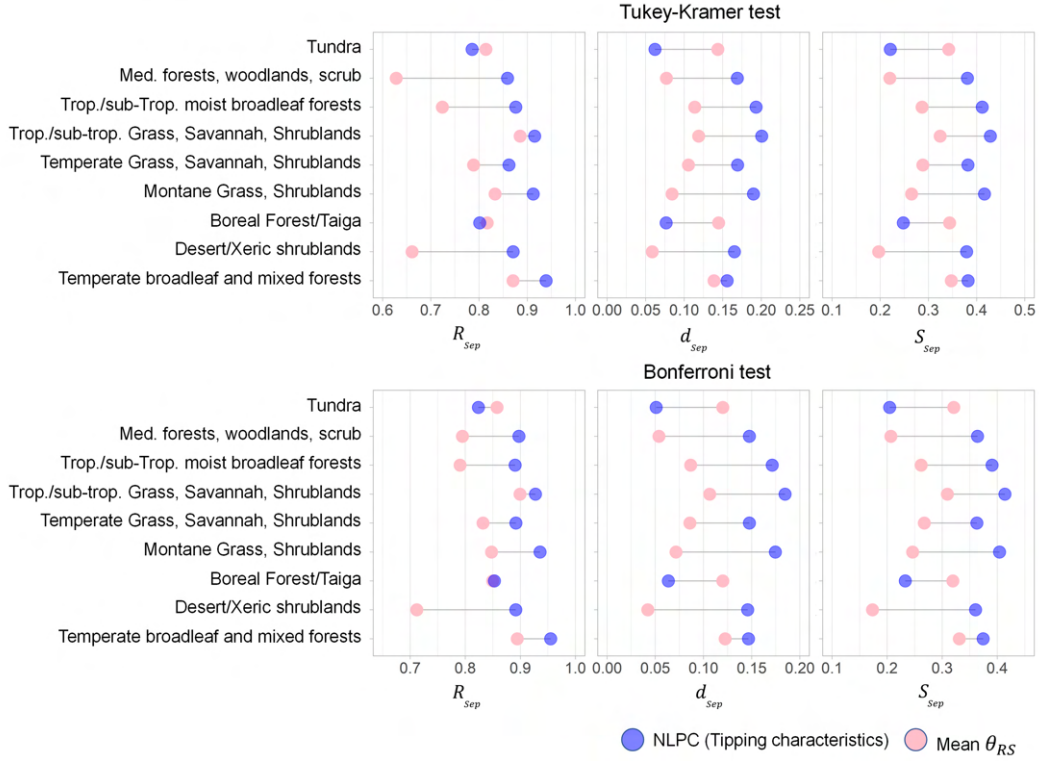
Precipitation characteristics can influence  $\eta$  primarily in two ways. First, storm intensity and subgrid distribution determines the post-storm hydrologic state of  $\theta_{RS}$ . Heavy and well distributed precipitation within the pixel can shift the hydrologic state of  $\theta_{RS}$  to wet or gravity drainage regime, thus initiating specific pathways for  $\theta_{RS}$  to return to dry-preferential state based on the post-storm  $\theta_{RS}$  conditions. Second, the inter-arrival period of precipitation controls the frequency of shift in the hydrologic state of  $\theta_{RS}$  from dry to wet preferential states. Hence,  $\eta$  shows high temporal variability as the precipitation characteristics change over seasons, with distinctively high values over boreal summer. As explained previously, arid regions are characterized by higher  $\bar{\tau}$ , the corresponding values of  $\eta$  are lower than other hydroclimates. Higher pixel clay content (>40%) corresponds with an increase in  $\eta$  values, indicating a potential linkage between the structure of clayey soils with the effective drydown rates of  $\theta_{RS}$  for the RS-footprint. High clay content is linked to higher potential for macropore formation in soils (Tang et al., 2023) which may lead to faster tipping of pixel to dry-preferential states.

Figure 11 shows a comparison of the  $R_{Sep}$ ,  $d_{Sep}$  and  $S_{Sep}$  of ecoregions for different biomes using NLPC and long-term mean  $\theta_{RS}$  (March'15 – September'21). The results indicate that NLPC is sensitive to inter-ecoregion differences within a biome, with global mean  $R_{Sep} = 0.87$  and  $0.90$ ,  $d_{Sep} = 0.15$  and  $0.14$ , and,  $S_{Sep} = 0.36$  and  $0.35$  using Tukey and Bonferroni tests respectively. Corresponding statistics using long-term mean  $\theta_{RS}$  show lower skill in partitioning in inter-ecoregion differences with  $R_{Sep} = 0.78$  and  $0.83$ ,  $d_{Sep} = 0.11$  and  $0.09$ , and,  $S_{Sep} = 0.29$  and  $0.27$ , respectively. For most biomes, including grasslands, savannah and shrublands, NLPC show a higher skill in partitioning ecoregions compared to  $\theta_{RS}$ . The difference in the results is more dramatic for Desert and Xeric biome, which are characterized by low mean  $\theta_{RS}$ . NLPC show a significant improvement in partitioning ecoregions within these biomes due to its sensitivity to transient changes in  $\theta_{RS}$  dynamics. For high latitude Tundra and Boreal forests, long-term mean  $\theta_{RS}$  shows a better skill in partitioning intra-biome ecoregions. This can be attributed to the uncertainty in parameterizing  $\theta_{RS}$  density distribution for these regions, which may be better parameterized using Truncated Weibull, as opposed to TG or TGM models used for simplicity (as shown in Figures S1 and S2 in Supplementary material). This may impact the estimation of tipping characteristics, and hence NLPC for these ecoregions. A global comparison of the long-term mean  $\theta_{RS}$  and NLPC is shown in Figure S8 of the Supplementary material.

## 4.6 Applications of $\theta_{RS}$ tipping characteristics

### 4.6.1 Global Earth-System /climate model diagnostics

Parameterization of global  $\theta_{RS}$  density distribution has obvious applications in characterizing  $\theta_{RS}$  extremes for flood and drought applications. Additionally, global coverage and sub-weekly temporal resolution make SMAP dataset valuable for a global scale performance assessment of climate and land- surface models. Previously, studies have proposed climate model assessment using SM density distribution (Vilasa et al., 2017), long- and short-term trends (Xi et al., 2022), or coupling strength of SM with hydrometeorological variables like temperature (Dong & Crow, 2018) and latent heat flux (Lei et al., 2018). However, the use of  $\theta_{RS}$  tipping characteristics in assessing global climate model simulations of SM can provide a more stringent approach for evaluating model accuracy. As soil texture and climate variability influences each tipping characteristics differently, simulation accuracy assessment of climate/ Earth System models using  $\theta_{RS}$  tipping characteristics can also help distinguish modeling error due to incorrect soil parameters and/or climate forcing.



**Figure 11.** Values of Separation fraction ( $R_{Sep}$ ), Separation distance ( $d_{Sep}$ ) and Separation score ( $S_{Sep}$ ) using (**Top**) Tukey-Kramer test and (**Bottom**) Bonferroni test for separation of inter-ecoregion NLPC means within global biomes. The blue and pink circles are used for NLPC (of  $\theta_{RS}$  tipping characteristics) and long-term (March 2015–September 2021) mean  $\theta_{RS}$  respectively. Only those ecoregions with a minimum of 100 data samples are included in the analysis.

#### 4.6.2 Quantifying ecosystem sensitivity to climate change

Changes in soil drying and rewetting cycles (in other words, hydrologic tipping characteristics) has been observed to impact the soil microbial community diversity, composition, and structure (Pesaro et al., 2004; Wang et al., 2022), and is demonstrated to have significant ecosystem level ramifications in their ability to alter the carbon and nitrogen cycles (Fierer & Schimel, 2002). Additionally soil wetting and drying cycles can have a significant impact on the soil-atmospheric carbon exchange, with implications for the climate change impacts on the ecosystems (Rousk & Brangari, 2022). Hence, tipping characteristics of  $\theta_{RS}$  can help develop novel insights in the relationship between dynamic changes in soil hydrologic states and its impacts on carbon and nitrogen cycle at landscape scale. Furthermore,  $\theta_{RS}$  tipping characteristics can be used to mapping regions of unique soil-vegetation-climate co-existence, which may serve as new fundamental units to discretize watersheds to regionalize soil hydraulic properties, vegetation response to moisture pulse, and multiscale interactions between the water, energy, and carbon cycle processes at landscape scales.

## 5 Summary and Conclusion

This study provides a global assessment of the preferential hydrologic states and tipping characteristics of  $\theta_{RS}$  using SMAP observations. Footprint-scale density distribution of the seasonal  $\theta_{RS}$  is parameterized globally based on the fitting performance of Truncated-gamma (unimodal) or Truncated-Gamma mixture (bimodal) models. The transition or tipping of  $\theta_{RS}$  from wet- to dry-average conditions, demarcated by a threshold  $\theta^X$ , determine the characterization of the preferential hydrologic state into wet-preferential (short, low intensity excursions into dry-average conditions), dry-preferential (long, high intensity excursions into dry-average conditions), or bistable (frequent, moderate excursions into dry-average conditions) states. Preferential hydrologic states are the physical manifestation of the dynamic shift of  $\theta_{RS}$  between wet and dry-average states which are controlled by climate and soil of the pixel, further moderated by subgrid-scale spatial distribution and variability in topography, vegetation, and initial  $\theta_{RS}$  conditions. The intensity, frequency, and duration of the excursion of  $\theta_{RS}$  into the dry-average conditions is characterized by three crossing properties, namely, *a*) Mean tipping depth,  $\bar{\varepsilon}[-]$ , *b*) Tipping Count,  $\eta[-]$  and *c*) Mean Tipped Time,  $\bar{\tau}$  [days]. While precipitation characteristics (distribution and interarrival frequency) regulate  $\bar{\varepsilon}$  and  $\eta$ , soil texture exerts strong influence over  $\bar{\tau}$  through control over drydown characteristics of  $\theta_{RS}$ .

Bistable hydrologic states of  $\theta_{RS}$  are prevalent in semi-arid and subhumid climates, generally overlapping with the regional of strong precipitation-SM coupling and monsoonal climate. Dry- and wet-preferential states of  $\theta_{RS}$  are observed over large fractions of global arid and humid regions respectively. Large temporal variability is observed in the spatial distribution of global  $\theta_{RS}$  preferential states primarily caused by changes in precipitation characteristics over the seasons. In the case of bimodal distributions, the dryer mode typically manifest close to the “*effective*” wilting point of the pixel, while the wet mode is observed at the threshold of the wet and transitional hydrologic regimes - a marked deviation from field studies due to the homogenization effect of the spatial variability in  $\theta_{RS}$  and its controls within the pixel. Climate regulates the threshold between the wet- and dry-average conditions. The density distribution modes of  $\theta_{RS}$  is moderated by soil texture, due to its control over water retention characteristics through increasing capillary matric potential, especially for the dry-preferential state or the dry mode of the bistable  $\theta_{RS}$  states. Global prevalence of bistable state of  $\theta_{RS}$  highlights that the representation of the temporal dynamics of  $\theta_{RS}$  with equilibrium-state mean  $\theta_{RS}$  may be incorrect as such values may correspond to a hydrologic state with relatively low probability.

The preferential hydrologic states along with the tipping characteristics constitute the emergent properties of  $\theta_{RS}$  dynamics at RS-footprint scale, with dynamic linkage to ter-

restrial hydrologic and energy flux partitioning, soil-vegetation-atmospheric coupling, and various bio-geo-chemical processes at multiple spatio-temporal scales. The proposed method of using preferential states to characterize large-scale  $\theta_{RS}$  dynamics is less prone to the observational constraints (satellite overpass frequency and resolution), and scaling effects due to land-surface heterogeneity in accurate identification of the thresholds of soil hydrologic regimes. Quantifying  $\theta_{RS}$  tipping characteristics provide a unique method to capture the coexistence of the climate, soil and vegetation linkages on effective SM dynamics, with potential applications in understanding vegetation response to SM stress, assessing climate change effects on soil processes and performance assessment of global climate/ Earth-System models.

## 6 Data Availability Statement

SMAP SM and soil texture data is available at NASA National Snow, and Ice Data Center Distributed Active Archive Center (NSIDC-DAAC): <http://nsidc.org/data/SPL3SMP>. The Aridity index is available at (30 arc-seconds) <https://cgiarcsi.community/data/global-aridity-and-pet-database/>. Global terrestrial ecoregions and biomes can be accessed from: <https://www.worldwildlife.org/publications/terrestrial-ecoregions-of-the-world>. Global estimates of surface soil texture are accessed from: <https://soilgrids.org/>. Global estimates of  $\theta_{RS}$  preferential hydrologic states, tipping characteristics and other variables discussed in this study are freely available in NetCDF format on HydroShare through the following resource: Sehgal, V. (2023). Characteristics of Global Surface Soil Moisture Preferential Hydrologic States, <http://www.hydroshare.org/resource/09da0247bed0447ba5476dacdfbaf658>

## Acknowledgments

The authors acknowledge the funding support from NASA SMAP projects (NNX16AQ58G, 80NSSC20K1807). We thank the Texas A&M High-Performance Research Computing (HPRC) for providing computing resource for the research.

## References

- Abdelkader, M., & Yerdelen, C. (2022, feb). Hydrological drought variability and its teleconnections with climate indices. *Journal of Hydrology*, 605, 127290. Retrieved from <https://doi.org/10.1016/j.jhydrol.2021.127290> doi: 10.1016/j.jhydrol.2021.127290
- Abramowitz, M., Stegun, I. A., & Romer, R. H. (1988, oct). *ihandbook of mathematical functions with formulas, graphs, and mathematical tables/i*. *American Journal of*

- Physics*, 56(10), 958–958. Retrieved from <https://doi.org/10.1119%2F1.15378>  
doi: 10.1119/1.15378
- Akbar, R., Gianotti, D. J. S., McColl, K. A., Haghghi, E., Salvucci, G. D., & Entekhabi, D. (2018, may). Estimation of landscape soil water losses from satellite observations of soil moisture. *Journal of Hydrometeorology*, 19(5), 871–889. Retrieved from <https://doi.org/10.1175%2Fjhm-d-17-0200.1> doi: 10.1175/jhm-d-17-0200.1
- Alessi, M. J., Herrera, D. A., Evans, C. P., DeGaetano, A. T., & Ault, T. R. (2022, mar). Soil moisture conditions determine land-atmosphere coupling and drought risk in the northeastern united states. *Journal of Geophysical Research: Atmospheres*, 127(6). Retrieved from <https://doi.org/10.1029%2F2021jd034740> doi: 10.1029/2021jd034740
- Ashman, K. A., Bird, C. M., & Zepf, S. E. (1994, dec). Detecting bimodality in astronomical datasets. *The Astronomical Journal*, 108, 2348. Retrieved from <https://doi.org/10.1086%2F117248> doi: 10.1086/117248
- Baldwin, D., Manfreda, S., Keller, K., & Smithwick, E. (2017, mar). Predicting root zone soil moisture with soil properties and satellite near-surface moisture data across the conterminous united states. *Journal of Hydrology*, 546, 393–404. Retrieved from <https://doi.org/10.1016%2Fj.jhydro.2017.01.020> doi: 10.1016/j.jhydro.2017.01.020
- Barton, E. J., Taylor, C. M., Parker, D. J., Turner, A. G., Belušić, D., BÅŕing, S. J., ... Mitra, A. K. (2019, apr). A case-study of land-atmosphere coupling during monsoon onset in northern india. *Quarterly Journal of the Royal Meteorological Society*, 146(731), 2891–2905. Retrieved from <https://doi.org/10.1002%2Fqj.3538> doi: 10.1002/qj.3538
- Baudena, M., D'Andrea, F., & Provenzale, A. (2008, dec). A model for soil-vegetation-atmosphere interactions in water-limited ecosystems. *Water Resources Research*, 44(12). Retrieved from <https://doi.org/10.1029%2F2008wr007172> doi: 10.1029/2008wr007172
- Bland, J. M., & Altman, D. G. (1995, jan). Statistics notes: Multiple significance tests: the bonferroni method. *BMJ*, 310(6973), 170–170. Retrieved from <https://doi.org/10.1136%2Fbmj.310.6973.170> doi: 10.1136/bmj.310.6973.170
- Burgin, M. S., Colliander, A., Njoku, E. G., Chan, S. K., Cabot, F., Kerr, Y. H., ... Yueh, S. H. (2017, may). A comparative study of the SMAP passive soil moisture product with existing satellite-based soil moisture products. *IEEE Transactions on Geoscience and Remote Sensing*, 55(5), 2959–2971. Retrieved from <https://doi.org/10.1109%2Ftgrs.2017.2656859> doi: 10.1109/tgrs.2017.2656859
- Burnham, K. P. (2002). Model selection and multimodel inference. *A practical information-*

- theoretic approach.*
- Cueto-Felgueroso, L., Dentz, M., & Juanes, R. (2015, may). Regime shifts in bistable water-stressed ecosystems due to amplification of stochastic rainfall patterns. *Physical Review E*, 91(5). Retrieved from <https://doi.org/10.1103/PhysRevE.91.052148> doi: 10.1103/physreve.91.052148
- Diamantaras, K. I., & Kung, S. Y. (1996). *Principal component neural networks: theory and applications*. John Wiley & Sons, Inc.
- Dirmeyer, P. A. (2011, aug). The terrestrial segment of soil moisture-climate coupling. *Geophysical Research Letters*, 38(16), n/a–n/a. Retrieved from <https://doi.org/10.1029/2011gl048268> doi: 10.1029/2011gl048268
- D'Odorico, P., & Porporato, A. (2004, jun). Preferential states in soil moisture and climate dynamics. *Proceedings of the National Academy of Sciences*, 101(24), 8848–8851. Retrieved from <https://doi.org/10.1073/pnas.0401428101> doi: 10.1073/pnas.0401428101
- D'Odorico, P., Ridolfi, L., Porporato, A., & Rodriguez-Iturbe, I. (2000, aug). Preferential states of seasonal soil moisture: The impact of climate fluctuations. *Water Resources Research*, 36(8), 2209–2219. Retrieved from <https://doi.org/10.1029/2000wr900103> doi: 10.1029/2000wr900103
- Dominguez, F., Kumar, P., & Vivoni, E. R. (2008, oct). Precipitation recycling variability and ecoclimatological stability—a study using NARR data. part II: North american monsoon region. *Journal of Climate*, 21(20), 5187–5203. Retrieved from <https://doi.org/10.1175/2008jcli1760.1> doi: 10.1175/2008jcli1760.1
- Dong, J., & Crow, W. T. (2018, dec). Use of satellite soil moisture to diagnose climate model representations of european soil moisture-air temperature coupling strength. *Geophysical Research Letters*, 45(23). Retrieved from <https://doi.org/10.1029/2018gl080547> doi: 10.1029/2018gl080547
- Dunn, O. J. (1961, mar). Multiple comparisons among means. *Journal of the American Statistical Association*, 56(293), 52–64. Retrieved from <https://doi.org/10.1080/2F01621459.1961.10482090> doi: 10.1080/01621459.1961.10482090
- Endsley, K. A., Kimball, J. S., Reichle, R. H., & Watts, J. D. (2020, dec). Satellite monitoring of global surface soil organic carbon dynamics using the SMAP level 4 carbon product. *Journal of Geophysical Research: Biogeosciences*, 125(12). Retrieved from <https://doi.org/10.1029/2020jg006100> doi: 10.1029/2020jg006100
- Entekhabi, D., Njoku, E. G., O'Neill, P. E., Kellogg, K. H., Crow, W. T., Edelstein, W. N., ... others (2010). The soil moisture active passive (smap) mission. *Proceedings of the IEEE*, 98(5), 704–716.
- Entekhabi, D., Rodriguez-Iturbe, I., & Bras, R. L. (1992, aug). Variability in large-scale

- water balance with land surface-atmosphere interaction. *Journal of Climate*, 5(8), 798–813. Retrieved from <https://doi.org/10.1175%2F1520-0442%281992%29005%3C0798%3Avilswb%3E2.0.co%3B2> doi: 10.1175/1520-0442(1992)005<0798:vilswb>2.0.co;2
- Entekhabi, D., Rodriguez-Iturbe, I., & Castelli, F. (1996, oct). Mutual interaction of soil moisture state and atmospheric processes. *Journal of Hydrology*, 184(1-2), 3–17. Retrieved from <https://doi.org/10.1016%2F0022-1694%2895%2902965-6> doi: 10.1016/0022-1694(95)02965-6
- Famiglietti, J. S., Ryu, D., Berg, A. A., Rodell, M., & Jackson, T. J. (2008). Field observations of soil moisture variability across scales. *Water Resources Research*, 44(1).
- Feldman, A. F., Gianotti, D. J. S., Trigo, I. F., Salvucci, G. D., & Entekhabi, D. (2019, dec). Satellite-based assessment of land surface energy partitioning–soil moisture relationships and effects of confounding variables. *Water Resources Research*, 55(12), 10657–10677. Retrieved from <https://doi.org/10.1029%2F2019wr025874> doi: 10.1029/2019wr025874
- Feldman, A. F., Gianotti, D. J. S., Trigo, I. F., Salvucci, G. D., & Entekhabi, D. (2022, jan). Observed landscape responsiveness to climate forcing. *Water Resources Research*, 58(1). Retrieved from <https://doi.org/10.1029%2F2021wr030316> doi: 10.1029/2021wr030316
- Feng, X., Porporato, A., & Rodriguez-Iturbe, I. (2015, feb). Stochastic soil water balance under seasonal climates. *Proceedings of the Royal Society A: Mathematical, Physical and Engineering Sciences*, 471(2174), 20140623. Retrieved from <https://doi.org/10.1098%2Frspa.2014.0623> doi: 10.1098/rspa.2014.0623
- Fernandez-Illescas, C. P., Porporato, A., Laio, F., & Rodriguez-Iturbe, I. (2001, dec). The ecohydrological role of soil texture in a water-limited ecosystem. *Water Resources Research*, 37(12), 2863–2872. Retrieved from <https://doi.org/10.1029%2F2000wr000121> doi: 10.1029/2000wr000121
- Fick, S. E., & Hijmans, R. J. (2017, oct). WorldClim 2: new 1-km spatial resolution climate surfaces for global land areas. *International Journal of Climatology*, 37(12), 4302–4315. Retrieved from <https://doi.org/10.1002%2Fjoc.5086> doi: 10.1002/joc.5086
- Fierer, N., & Schimel, J. P. (2002, jun). Effects of drying–rewetting frequency on soil carbon and nitrogen transformations. *Soil Biology and Biochemistry*, 34(6), 777–787. Retrieved from <https://doi.org/10.1016%2Fs0038-0717%2802%2900007-x> doi: 10.1016/s0038-0717(02)00007-x
- Fu, Z., Ciais, P., Feldman, A. F., Gentine, P., Makowski, D., Prentice, I. C., ... Wigneron,

- J.-P. (2022, nov). Critical soil moisture thresholds of plant water stress in terrestrial ecosystems. *Science Advances*, 8(44). Retrieved from <https://doi.org/10.1126/2Fsciadv.abq7827> doi: 10.1126/sciadv.abq7827
- Fu, Z., Ciais, P., Makowski, D., Bastos, A., Stoy, P. C., Ibrom, A., ... Wigneron, J.-P. (2021, dec). Uncovering the critical soil moisture thresholds of plant water stress for european ecosystems. *Global Change Biology*, 28(6), 2111–2123. Retrieved from <https://doi.org/10.1111/2Fgcb.16050> doi: 10.1111/gcb.16050
- Gallego-Elvira, B., Taylor, C. M., Harris, P. P., Ghent, D., Veal, K. L., & Folwell, S. S. (2016, mar). Global observational diagnosis of soil moisture control on the land surface energy balance. *Geophysical Research Letters*, 43(6), 2623–2631. Retrieved from <https://doi.org/10.1002/2F2016gl068178> doi: 10.1002/2016gl068178
- Gantner, L., & Kalthoff, N. (2009, jun). Sensitivity of a modelled life cycle of a mesoscale convective system to soil conditions over west africa. *Quarterly Journal of the Royal Meteorological Society*, 136(S1), 471–482. Retrieved from <https://doi.org/10.1002/2Fqj.425> doi: 10.1002/qj.425
- Ghannam, K., Nakai, T., Paschalis, A., Oishi, C. A., Kotani, A., Igarashi, Y., ... Katul, G. G. (2016, feb). Persistence and memory timescales in root-zone soil moisture dynamics. *Water Resources Research*, 52(2), 1427–1445. Retrieved from <https://doi.org/10.1002/2F2015wr017983> doi: 10.1002/2015wr017983
- Hengl, T., de Jesus, J. M., Heuvelink, G. B. M., Gonzalez, M. R., Kilibarda, M., Blagotić, A., ... Kempen, B. (2017, feb). SoilGrids250m: Global gridded soil information based on machine learning. *PLOS ONE*, 12(2), e0169748. Retrieved from <https://doi.org/10.1371/2Fjournal.pone.0169748> doi: 10.1371/journal.pone.0169748
- Jackson, T., O'Neill, P., Chan, S., Bindlish, R., Colliander, A., Chen, F., & Dunbar, S. (2018). *Soil moisture active passive (smap) project: Calibration and validation for the l2/3sm<sub>p</sub>version5andl2/3sm<sub>p</sub>version2dataproductscitation (Tech. Rep.)*.
- Jacobs, E. M., Bertassello, L. E., & Rao, P. S. C. (2020, jan). Drivers of regional soil water storage memory and persistence. *Vadose Zone Journal*, 19(1). Retrieved from <https://doi.org/10.1002/2Fvzj2.20050> doi: 10.1002/vzj2.20050
- Kolassa, J., Reichle, R., Liu, Q., Alemohammad, S., Gentine, P., Aida, K., ... Walker, J. (2018, jan). Estimating surface soil moisture from SMAP observations using a neural network technique. *Remote Sensing of Environment*, 204, 43–59. Retrieved from <https://doi.org/10.1016/2Fj.rse.2017.10.045> doi: 10.1016/j.rse.2017.10.045
- Koster, R. D., Dirmeyer, P. A., Guo, Z., Bonan, G., Chan, E., Cox, P., ... Yamada, T. (2004, aug). Regions of strong coupling between soil moisture and precipitation. *Science*, 305(5687), 1138–1140. Retrieved from <https://doi.org/10.1126/2Fscience.1100217> doi: 10.1126/science.1100217

- Kramer, M. A. (1991, feb). Nonlinear principal component analysis using autoassociative neural networks. *AIChE Journal*, *37*(2), 233–243. Retrieved from <https://doi.org/10.1002/aic.690370209> doi: 10.1002/aic.690370209
- Kumar, T. L., Durga, G. P., Rao, K. K., Nagendra, H., & Mall, R. (2021). Moisture recycling over the indian monsoon core region in response to global warming from CMIP5 models. In *Indian summer monsoon variability* (pp. 449–466). Elsevier. Retrieved from <https://doi.org/10.1016/b978-0-12-822402-1.00008-9> doi: 10.1016/b978-0-12-822402-1.00008-9
- Kurita, N., & Yamada, H. (2008, aug). The role of local moisture recycling evaluated using stable isotope data from over the middle of the tibetan plateau during the monsoon season. *Journal of Hydrometeorology*, *9*(4), 760–775. Retrieved from <https://doi.org/10.1175/2007jhm945.1> doi: 10.1175/2007jhm945.1
- Laio, F., Porporato, A., Ridolfi, L., & Rodriguez-Iturbe, I. (2001, jul). Plants in water-controlled ecosystems: active role in hydrologic processes and response to water stress. *Advances in Water Resources*, *24*(7), 707–723. Retrieved from [https://doi.org/10.1016/s0309-1708\(01\)00005-7](https://doi.org/10.1016/s0309-1708(01)00005-7) doi: 10.1016/s0309-1708(01)00005-7
- Lee, E., & Kim, S. (2022, feb). Spatiotemporal soil moisture response and controlling factors along a hillslope. *Journal of Hydrology*, *605*, 127382. Retrieved from <https://doi.org/10.1016/j.jhydrol.2021.127382> doi: 10.1016/j.jhydrol.2021.127382
- Lee, S., & Lee, D. K. (2018, oct). What is the proper way to apply the multiple comparison test? *Korean Journal of Anesthesiology*, *71*(5), 353–360. Retrieved from <https://doi.org/10.4097/kja.d.18.00242> doi: 10.4097/kja.d.18.00242
- Lee, T. R., & Hornberger, G. M. (2006). Inferred bimodality in the distribution of soil moisture at big meadows, shenandoah national park, virginia. *Geophysical Research Letters*, *33*(6). Retrieved from <https://doi.org/10.1029/2005gl025536> doi: 10.1029/2005gl025536
- Lei, F., Crow, W. T., Holmes, T. R. H., Hain, C., & Anderson, M. C. (2018, oct). Global investigation of soil moisture and latent heat flux coupling strength. *Water Resources Research*, *54*(10), 8196–8215. Retrieved from <https://doi.org/10.1029/2018wr023469> doi: 10.1029/2018wr023469
- Lohou, F., Kergoat, L., Guichard, F., Boone, A., Cappelaere, B., Cohard, J.-M., ... Timouk, F. (2014, apr). Surface response to rain events throughout the west african monsoon. *Atmospheric Chemistry and Physics*, *14*(8), 3883–3898. Retrieved from <https://doi.org/10.5194/acp-14-3883-2014> doi: 10.5194/acp-14-3883-2014
- Manfreda, S., Scanlon, T. M., & Caylor, K. K. (2009). On the importance of accurate depiction of infiltration processes on modelled soil moisture and vegetation water stress. *Ecohydrology*, n/a–n/a. Retrieved from <https://doi.org/10.1002/eco.79> doi: 10.1002/eco.79

- 10.1002/eco.79
- McColl, K. A., Wang, W., Peng, B., Akbar, R., Gianotti, D. J. S., Lu, H., . . . Entekhabi, D. (2017, apr). Global characterization of surface soil moisture drydowns. *Geophysical Research Letters*, *44*(8), 3682–3690. Retrieved from <https://doi.org/10.1002/2F2017gl1072819> doi: 10.1002/2017gl1072819
- Miró, J. J., Caselles, V., & Estrela, M. J. (2017, nov). Multiple imputation of rainfall missing data in the iberian mediterranean context. *Atmospheric Research*, *197*, 313–330. Retrieved from <https://doi.org/10.1016%2Fj.atmosres.2017.07.016> doi: 10.1016/j.atmosres.2017.07.016
- Monahan, A. H. (2000, feb). Nonlinear principal component analysis by neural networks: Theory and application to the lorenz system. *Journal of Climate*, *13*(4), 821–835. Retrieved from <https://doi.org/10.1175%2F1520-0442%282000%29013%3C0821%3Anpcabn%3E2.0.co%3B2> doi: 10.1175/1520-0442(2000)013<0821:npcabn>2.0.co;2
- Nazareth, J. L. (2009, jul). Conjugate gradient method. *WIREs Computational Statistics*, *1*(3), 348–353. Retrieved from <https://doi.org/10.1002%2Fwics.13> doi: 10.1002/wics.13
- Nishat, S., Guo, Y., & Baetz, B. (2007, aug). Development of a simplified continuous simulation model for investigating long-term soil moisture fluctuations. *Agricultural Water Management*, *92*(1-2), 53–63. Retrieved from <https://doi.org/10.1016%2Fj.agwat.2007.04.012> doi: 10.1016/j.agwat.2007.04.012
- Oglesby, R. J. (2002). Thresholds in atmosphere–soil moisture interactions: Results from climate model studies. *Journal of Geophysical Research*, *107*(D14). Retrieved from <https://doi.org/10.1029%2F2001jd001045> doi: 10.1029/2001jd001045
- Olson, D. M., Dinerstein, E., Wikramanayake, E. D., Burgess, N. D., Powell, G. V. N., Underwood, E. C., . . . Kassem, K. R. (2001). Terrestrial ecoregions of the world: A new map of life on earth. *BioScience*, *51*(11), 933. Retrieved from <https://doi.org/10.1641%2F0006-3568%282001%29051%5B0933%3Ateotwa%5D2.0.co%3B2> doi: 10.1641/0006-3568(2001)051[0933:teotwa]2.0.co;2
- O’Neill. (2018). *Smap l3 radiometer global daily 36 km ease-grid soil moisture, version 5* (Tech. Rep.). doi: <https://doi.org/10.5067/ZX7YX2Y2LHEB>
- Pathak, A., Ghosh, S., & Kumar, P. (2014, sep). Precipitation recycling in the indian subcontinent during summer monsoon. *Journal of Hydrometeorology*, *15*(5), 2050–2066. Retrieved from <https://doi.org/10.1175%2Fjhm-d-13-0172.1> doi: 10.1175/jhm-d-13-0172.1
- Pendergrass, A. G., Meehl, G. A., Pulwarty, R., Hobbins, M., Hoell, A., AghaKouchak, A., . . . Woodhouse, C. A. (2020, mar). Flash droughts present a new challenge for subseasonal-to-seasonal prediction. *Nature Climate Change*, *10*(3), 191–199. Retrieved

- from <https://doi.org/10.1038%2Fs41558-020-0709-0> doi: 10.1038/s41558-020-0709-0
- Pesaro, M., Nicollier, G., Zeyer, J., & Widmer, F. (2004, may). Impact of soil drying-rewetting stress on microbial communities and activities and on degradation of two crop protection products. *Applied and Environmental Microbiology*, *70*(5), 2577–2587. Retrieved from <https://doi.org/10.1128%2Faem.70.5.2577-2587.2004> doi: 10.1128/aem.70.5.2577-2587.2004
- Porporato, A., Daly, E., & Rodriguez-Iturbe, I. (2004, nov). Soil water balance and ecosystem response to climate change. *The American Naturalist*, *164*(5), 625–632. Retrieved from <https://doi.org/10.1086%2F424970> doi: 10.1086/424970
- Porporato, A., D’Odorico, P., Laio, F., Ridolfi, L., & Rodriguez-Iturbe, I. (2002, aug). Ecohydrology of water-controlled ecosystems. *Advances in Water Resources*, *25*(8-12), 1335–1348. Retrieved from <https://doi.org/10.1016%2Fs0309-1708%2802%2900058-1> doi: 10.1016/s0309-1708(02)00058-1
- Rafter, J. A., Abell, M. L., & Braselton, J. P. (2002, jan). Multiple comparison methods for means. *SIAM Review*, *44*(2), 259–278. Retrieved from <https://doi.org/10.1137%2Fs0036144501357233> doi: 10.1137/s0036144501357233
- Ray, R. L., Jacobs, J. M., & Ballesterio, T. P. (2011, may). Regional landslide susceptibility: spatiotemporal variations under dynamic soil moisture conditions. *Natural Hazards*, *59*(3), 1317–1337. Retrieved from <https://doi.org/10.1007%2Fs11069-011-9834-4> doi: 10.1007/s11069-011-9834-4
- Razavi, T., & Coulibaly, P. (2013, jun). Classification of ontario watersheds based on physical attributes and streamflow series. *Journal of Hydrology*, *493*, 81–94. Retrieved from <https://doi.org/10.1016%2Fj.jhydro1.2013.04.013> doi: 10.1016/j.jhydro1.2013.04.013
- Razavi, T., & Coulibaly, P. (2016, jun). An evaluation of regionalization and watershed classification schemes for continuous daily streamflow prediction in ungauged watersheds. *Canadian Water Resources Journal / Revue canadienne des ressources hydriques*, *42*(1), 2–20. Retrieved from <https://doi.org/10.1080%2F07011784.2016.1184590> doi: 10.1080/07011784.2016.1184590
- Reichle, R. H., De Lannoy, G. J. M., Liu, Q., Colliander, A., Conaty, A., Jackson, T., ... Koster, R. D. (2015). *Technical report series on global modeling and data assimilation, volume 40 soil moisture active passive (smap) project assessment report for the beta-release l4\_smdataproduct (Vol. 40;Tech. Rep.)*.
- Rodriguez-Iturbe, I. (2000, jan). Ecohydrology: A hydrologic perspective of climate-soil-vegetation dynamics. *Water Resources Research*, *36*(1), 3–9. Retrieved from <https://doi.org/10.1029%2F1999wr900210> doi: 10.1029/1999wr900210

- Rodriguez-Iturbe, I., Entekhabi, D., & Bras, R. L. (1991). Nonlinear dynamics of soil moisture at climate scales: 1. stochastic analysis. *Water Resources Research*, *27*(8), 1899–1906.
- Rodríguez-Iturbe, I., & Porporato, A. (2007). *Ecohydrology of water-controlled ecosystems: soil moisture and plant dynamics*. Cambridge University Press.
- Rodriguez-Iturbe, I., Porporato, A., Laio, F., & Ridolfi, L. (2001, dec). Intensive or extensive use of soil moisture: Plant strategies to cope with stochastic water availability. *Geophysical Research Letters*, *28*(23), 4495–4497. Retrieved from <https://doi.org/10.1029%2F2001gl012905> doi: 10.1029/2001gl012905
- Rodriguez-Iturbe, I., Porporato, A., Ridolfi, L., Isham, V., & Coxi, D. R. (1999, oct). Probabilistic modelling of water balance at a point: the role of climate, soil and vegetation. *Proceedings of the Royal Society of London. Series A: Mathematical, Physical and Engineering Sciences*, *455*(1990), 3789–3805. Retrieved from <https://doi.org/10.1098%2Frspa.1999.0477> doi: 10.1098/rspa.1999.0477
- Rousk, J., & Brangari, A. (2022, mar). Do the respiration pulses induced by drying–rewetting matter for the soil–atmosphere carbon balance? *Global Change Biology*, *28*(11), 3486–3488. Retrieved from <https://doi.org/10.1111%2Fgcb.16163> doi: 10.1111/gcb.16163
- Ruxton, G. D., & Beauchamp, G. (2008). Time for some a priori thinking about post hoc testing. *Behavioral Ecology*, *19*(3), 690–693. Retrieved from <https://doi.org/10.1093%2Fbeheco%2Farn020> doi: 10.1093/beheco/arn020
- Sadri, S., Pan, M., Wada, Y., Vergopolan, N., Sheffield, J., Famiglietti, J. S., ... Wood, E. (2020, sep). A global near-real-time soil moisture index monitor for food security using integrated SMOS and SMAP. *Remote Sensing of Environment*, *246*, 111864. Retrieved from <https://doi.org/10.1016%2Fj.rse.2020.111864> doi: 10.1016/j.rse.2020.111864
- Santanello, J. A., Dirmeyer, P. A., Ferguson, C. R., Findell, K. L., Tawfik, A. B., Berg, A., ... Wulfmeyer, V. (2018, jun). Land–atmosphere interactions: The LoCo perspective. *Bulletin of the American Meteorological Society*, *99*(6), 1253–1272. Retrieved from <https://doi.org/10.1175%2Fbams-d-17-0001.1> doi: 10.1175/bams-d-17-0001.1
- Sardooi, E. R., Azareh, A., Choubin, B., Barkhori, S., Singh, V. P., & Shamshirband, S. (2019, oct). Applying the remotely sensed data to identify homogeneous regions of watersheds using a pixel-based classification approach. *Applied Geography*, *111*, 102071. Retrieved from <https://doi.org/10.1016%2Fj.apgeog.2019.102071> doi: 10.1016/j.apgeog.2019.102071
- Scheffer, M., Carpenter, S., Foley, J. A., Folke, C., & Walker, B. (2001, oct). Catastrophic shifts in ecosystems. *Nature*, *413*(6856), 591–596. Retrieved from <https://doi.org/>

- 10.1038/35098000 doi: 10.1038/35098000
- Scholz, M. (2012, mar). Validation of nonlinear PCA. *Neural Processing Letters*, *36*(1), 21–30. Retrieved from <https://doi.org/10.1007/s11063-012-9220-6> doi: 10.1007/s11063-012-9220-6
- Scholz, M., Fraunholz, M., & Selbig, J. (2008). Nonlinear principal component analysis: Neural network models and applications. In *Lecture notes in computational science and engineering* (pp. 44–67). Springer Berlin Heidelberg. Retrieved from [https://doi.org/10.1007/978-3-540-73750-6\\_2](https://doi.org/10.1007/978-3-540-73750-6_2) doi: 10.1007/978-3-540-73750-6\_2
- Scholz, M., Kaplan, F., Guy, C. L., Kopka, J., & Selbig, J. (2005, aug). Non-linear PCA: a missing data approach. *Bioinformatics*, *21*(20), 3887–3895. Retrieved from <https://doi.org/10.1093/bioinformatics/bti634> doi: 10.1093/bioinformatics/bti634
- Schwingshackl, C., Hirschi, M., & Seneviratne, S. I. (2017, aug). Quantifying spatiotemporal variations of soil moisture control on surface energy balance and near-surface air temperature. *Journal of Climate*, *30*(18), 7105–7124. Retrieved from <https://doi.org/10.1175/jcli-d-16-0727.1> doi: 10.1175/jcli-d-16-0727.1
- Sehgal, V., Gaur, N., & Mohanty, B. P. (2021a, aug). Global flash drought monitoring using surface soil moisture. *Water Resources Research*, *57*(9). Retrieved from <https://doi.org/10.1029/2021wr029901> doi: 10.1029/2021wr029901
- Sehgal, V., Gaur, N., & Mohanty, B. P. (2021b, jan). Global surface soil moisture drydown patterns. *Water Resources Research*, *57*(1). Retrieved from <https://doi.org/10.1029/2020wr027588> doi: 10.1029/2020wr027588
- Seneviratne, S. I., Corti, T., Davin, E. L., Hirschi, M., Jaeger, E. B., Lehner, I., . . . Teuling, A. J. (2010, may). Investigating soil moisture–climate interactions in a changing climate: A review. *Earth-Science Reviews*, *99*(3-4), 125–161. Retrieved from <https://doi.org/10.1016/j.earscirev.2010.02.004> doi: 10.1016/j.earscirev.2010.02.004
- Settin, T., Botter, G., Rodriguez-Iturbe, I., & Rinaldo, A. (2007, may). Numerical studies on soil moisture distributions in heterogeneous catchments. *Water Resources Research*, *43*(5). Retrieved from <https://doi.org/10.1029/2006wr005737> doi: 10.1029/2006wr005737
- Sheffield, J. (2004). A simulated soil moisture based drought analysis for the united states. *Journal of Geophysical Research*, *109*(D24). Retrieved from <https://doi.org/10.1029/2004jd005182> doi: 10.1029/2004jd005182
- Smith, R., Velhuis, H., Mills, G., Eilers, R., Fraser, W., & Lelyk, G. (1998). Terrestrial eozones, ecoregions, and ecodistricts of manitoba. *Technical bulletin*, *9*.
- Sujith, K., Saha, S. K., Pokhrel, S., Hazra, A., & Chaudhari, H. S. (2017, oct). The dominant

- modes of recycled monsoon rainfall over india. *Journal of Hydrometeorology*, 18(10), 2647–2657. Retrieved from <https://doi.org/10.1175%2Fjhm-d-17-0082.1> doi: 10.1175/jhm-d-17-0082.1
- Tamea, S., Laio, F., Ridolfi, L., & Rodriguez-Iturbe, I. (2011, sep). Crossing properties for geophysical systems forced by poisson noise. *Geophysical Research Letters*, 38(18), n/a–n/a. Retrieved from <https://doi.org/10.1029%2F2011gl049074> doi: 10.1029/2011gl049074
- Tang, C.-S., Cheng, Q., Gong, X., Shi, B., & Inyang, H. I. (2023, jan). Investigation on microstructure evolution of clayey soils: A review focusing on wetting/drying process. *Journal of Rock Mechanics and Geotechnical Engineering*, 15(1), 269–284. Retrieved from <https://doi.org/10.1016%2Fj.jrmge.2022.02.004> doi: 10.1016/j.jrmge.2022.02.004
- Taylor, C. M., de Jeu, R. A. M., Guichard, F., Harris, P. P., & Dorigo, W. A. (2012, sep). Afternoon rain more likely over drier soils. *Nature*, 489(7416), 423–426. Retrieved from <https://doi.org/10.1038%2Fnature11377> doi: 10.1038/nature11377
- Teuling, A. J. (2005). On bimodality in warm season soil moisture observations. *Geophysical Research Letters*, 32(13). Retrieved from <https://doi.org/10.1029%2F2005gl023223> doi: 10.1029/2005gl023223
- Tian, F., Wigneron, J.-P., Ciais, P., Chave, J., Ogée, J., Peñuelas, J., . . . Fensholt, R. (2018, aug). Coupling of ecosystem-scale plant water storage and leaf phenology observed by satellite. *Nature Ecology & Evolution*, 2(9), 1428–1435. Retrieved from <https://doi.org/10.1038%2Fs41559-018-0630-3> doi: 10.1038/s41559-018-0630-3
- Tuttle, S., & Salvucci, G. (2016, may). Empirical evidence of contrasting soil moisture–precipitation feedbacks across the united states. *Science*, 352(6287), 825–828. Retrieved from <https://doi.org/10.1126%2Fscience.aaa7185> doi: 10.1126/science.aaa7185
- UNEP. (1997). *World atlas of desertification* (Tech. Rep.). London ;. 1997. (Bibliography: p. 171-180.)
- Vilasa, L., Miralles, D. G., de Jeu, R. A. M., & Dolman, A. J. (2017, apr). Global soil moisture bimodality in satellite observations and climate models. *Journal of Geophysical Research: Atmospheres*, 122(8), 4299–4311. Retrieved from <https://doi.org/10.1002%2F2016jd026099> doi: 10.1002/2016jd026099
- Wang, X.-B., Azarbad, H., Leclerc, L., Dozois, J., Mukula, E., & Yergeau, É. (2022, aug). A drying-rewetting cycle imposes more important shifts on soil microbial communities than does reduced precipitation. *mSystems*, 7(4). Retrieved from <https://doi.org/10.1128%2Fmsystems.00247-22> doi: 10.1128/msystems.00247-22
- Xi, X., Gentine, P., Zhuang, Q., & Kim, S. (2022, mar). Evaluating the variability

- of surface soil moisture simulated within CMIP5 using SMAP data. *Journal of Geophysical Research: Atmospheres*, 127(5). Retrieved from <https://doi.org/10.1029%2F2021jd035363> doi: 10.1029/2021jd035363
- Yin, J., Porporato, A., & Albertson, J. (2014, jul). Interplay of climate seasonality and soil moisture-rainfall feedback. *Water Resources Research*, 50(7), 6053–6066. Retrieved from <https://doi.org/10.1002%2F2013wr014772> doi: 10.1002/2013wr014772
- Yu, Y., Notaro, M., Wang, F., Mao, J., Shi, X., & Wei, Y. (2017, nov). Observed positive vegetation-rainfall feedbacks in the sahel dominated by a moisture recycling mechanism. *Nature Communications*, 8(1). Retrieved from <https://doi.org/10.1038%2Fs41467-017-02021-1> doi: 10.1038/s41467-017-02021-1
- Zarnetske, J. P., Bouda, M., Abbott, B. W., Saiers, J., & Raymond, P. A. (2018, nov). Generality of hydrologic transport limitation of watershed organic carbon flux across ecoregions of the united states. *Geophysical Research Letters*, 45(21). Retrieved from <https://doi.org/10.1029%2F2018gl080005> doi: 10.1029/2018gl080005
- Zeppetello, L. R. V., Battisti, D. S., & Baker, M. B. (2019, sep). The origin of soil moisture evaporation “regimes”. *Journal of Climate*, 32(20), 6939–6960. Retrieved from <https://doi.org/10.1175%2Fjcli-d-19-0209.1> doi: 10.1175/jcli-d-19-0209.1
- Zhou, Y., Narumalani, S., Waltman, W. J., Waltman, S. W., & Palecki, M. A. (2003, jun). A GIS-based spatial pattern analysis model for eco-region mapping and characterization. *International Journal of Geographical Information Science*, 17(5), 445–462. Retrieved from <https://doi.org/10.1080%2F1365881031000086983> doi: 10.1080/1365881031000086983
- Zomer, R. J., Xu, J., & Trabucco, A. (2022). Version 3 of the global aridity index and potential evapotranspiration database. *Scientific Data*, 9(1), 409.